Bioactive Materials 42 (2024) 628–643

Contents lists available at ScienceDirect

Bioactive Materials

journal homepage: www.keaipublishing.com/en/journals/bioactive-materials

Baiting bacteria with amino acidic and peptidic corona coated defect-engineered antimicrobial nanoclusters for optimized wound healing

Maonan Wang [a,b,**,1], Houjuan Zhu [a,c,***,1], Yuling Xue [a], Yanxia Duan [b], Hua Tian [a], Qi Liu [b], Yuzhu Zhang [b], Zibiao Li [c], Xian Jun Loh [c], Enyi Ye [c], Gang Yin [b], Xuemei Wang [d], Xianguang Ding [e], David Tai Leong [a,*]

[a] Department of Chemical and Biomolecular Engineering, Faculty of Engineering, National University of Singapore, Singapore, 117585, Singapore
[b] Department of Pathology, Xiangya Hospital, School of Basic Medical Sciences, Central South University, Changsha, China
[c] Institute of Materials Research and Engineering (IMRE), Agency for Science, Technology and Research (A*STAR), 2 Fusionopolis Way, Innovis #08-03, Singapore, 138634, Singapore
[d] State Key Laboratory of Bioelectronics (Chien-Shiung Wu Lab), School of Biological Science and Medical Engineering, Southeast University, Nanjing, 210096, China
[e] Key Laboratory for Organic Electronics and Information Displays & Jiangsu Key Laboratory for Biosensors, Nanjing University of Posts & Telecommunications, Nanjing, 210023, China

ARTICLE INFO

Keywords:
Defect-engineered
Photothermal effect
Chemodynamic effect
Copper sulfide nanoclusters
Protein corona

ABSTRACT

Keeping steps ahead of the bacteria in the race for more efficacious antibacterial strategies is increasingly difficult with the advent of bacterial resistance genes. Herein, we engineered copper sulfide nanoclusters (CuS_x NCs) with variable sulfur defects for enhanced dual-treatment of bacterial infections by manipulating photothermal effects and Fenton-like activity. Next, by encasing CuS_x NCs with a complex mixture of amino acids and short peptides derived from Luria-Bertani bacterial culture media as a protein corona, we managed to coax E. Coli to take up these CuS_x NCs. As a whole, Amino-Pep-CuS_x NCs was perceived as a food source and actively consumed by bacteria, enhancing their effective uptake by at least 1.5-fold greater than full length BSA protein BSA-corona CuS_x NCs. Through strategically using defect-engineering, we successfully fine-tune photothermal effect and Fenton-like capacity of CuS_x NCs. Increased sulfur defects lead to reduced but sufficient heat generation under solar-light irradiation and increased production of toxic hydroxyl radicals. By fine-tuning sulfur defects during synthesis, we achieve CuS_x NCs with an optimal synergistic effect, significantly enhancing their bactericidal properties. These ultra-small and biodegradable CuS_x NCs can rapidly break down after treatment for clearance. Thus, Amino-Pep-CuS_x NCs demonstrate effective eradication of bacteria both *in vitro* and *in vivo* because of their relatively high uptake, optimal balanced photothermal and chemodynamic outcomes. Our study offers a straightforward and efficient method to enhance bacterial uptake of next generation of antibacterial agents.

1. Introduction

Bacteria are ubiquitous microorganisms found throughout nature, existing in nearly every environment [1–3]. Despite the development of various methods to eradicate bacteria, bacterial infections persist [4–6]. Bacterial toxins pose a global health concern; for instance, according to the CDC, Escherichia coli (*E. coli*) and Staphylococcus aureus (*S. aureus*) remain the top two causes of infections [7–10]. Antibiotics are potent medications capable of combating bacterial infections. However, the inappropriate use, overuse, and mishandling of antibiotics contribute to the emergence of bacterial resistance [11,12]. The advancement of multiple antibiotics or the delivery of antibiotics through nanomaterials,

Peer review under responsibility of KeAi Communications Co., Ltd.
* Corresponding author.
** Corresponding author.
*** Corresponding author.
E-mail addresses: maonanwang@csu.edu.cn (M. Wang), zhu_houjuan@imre.a-star.edu.sg (H. Zhu), cheltwd@nus.edu.sg (D.T. Leong).
[1] Equal contribution.

https://doi.org/10.1016/j.bioactmat.2024.09.010
Received 21 June 2024; Received in revised form 22 August 2024; Accepted 6 September 2024

targeting individual drug-resistant bacteria, has, to some extent, expedited the evolution of drug-resistant strains [13–15]. The quest for a universal bactericidal approach appears aimed at bypassing the accelerated mutational escape of bacteria occurring during the bactericidal process. Drug-resistant bacteria can endure and proliferate in the presence of antibiotics, leading to a limited lifespan for these medications. Compounding the issue, individuals may only have a remaining window of ten to twenty years to utilize existing antibiotics, and the imminent development of new biocides becomes crucial [16–19].

Fenton-like catalysts, particularly those based on multivalent metals like titanium, copper, and manganese, play a crucial role in activating hydrogen peroxide (H_2O_2) to generate reactive oxygen species (ROS) for the degradation of organic pollutants in wastewater, chemodynamic apoptosis of cell in tumour treatment, and anti-bacteria in infectious wound [20–23]. Among these catalysts, copper-containing catalysts are especially noteworthy due to their cost-effectiveness, abundant availability, and ease of preparation [24]. Unlike iron-based catalysts, which are commonly used in traditional Fenton reactions, copper (Cu(II)) offers several advantages: (1) wider pH range: Cu(II) can effectively function as a Fenton-like catalyst across a broader pH range (3–9), making it more versatile in various environmental conditions; (2) lower risk of impurities: The Cu(II)/H_2O_2 system is less prone to generating unwanted by-products compared to the Fe(II)/H_2O_2 system; (3) higher efficiency in ROS formation: The Cu(I)/H_2O_2 system more readily forms hydroxyl radicals (HO•), which are highly reactive and effective in chemodynamic effect induced anti-bacteria [25]. Thus, these properties make copper-containing catalysts a promising alternative to traditional iron-based catalysts in Fenton-like reactions for treating infectious wound. Chemodynamic-photothermal dualistic antimicrobial modal nanoclusters can give a fast killing blow that is intentionally decoupled temporally from the often-slower genetic mutational driven antibiotic resistance [26–35]. These direct bactericide action with these nanoclusters do not exacerbate intrinsic bacterial resistance, suggesting a potential way to overcome the chemoresistance observed in lysozyme and antimicrobial peptides [36–38].

Copper-based nanomaterials find extensive use in biomedical applications owing to their commendable biocompatibility, efficient photothermal conversion, and cost-effectiveness [39,40]. Numerous researchers are actively engaged in enhancing the antimicrobial properties of CuS and many other nanomaterials though synergistic photothermal and chemodynamic effect [37,41–47].

Thus more often than not, the bottleneck in many highly efficacious antimicrobial effects may not be on their lethality but at the uptake aspects [48]. Some studies have found that wrapping biomaterials around the outside of nanomaterials enhances uptake, for example, in 2017, Jia et al. have found that wrapping glucose around pesticide nanoparticles enhances active cellular uptake of insecticides [49]. In 2020, Cao et al. found that polyvinylpyrrolidone (PVP)-coated iron oxide nanoparticles (NPs) significantly facilitated the intracellular transport of cadmium, possibly because the bacteria treated the nanoparticles as nutrients [50]. Here, we recognized that while bacteria have internal metabolic pathways to synthesize amino acids which are essential molecules for the bacterial fundamental cellular maintenance and cell division. However, during synthesis of the amino acids, even with all the endogeneous genetic machinery, the bacteria still needs a carbon source. In a bacterial infected wound, that carbon source comes from the blood plasma that contains a rich pool of proteins which the bacteria can digest to shorter peptides and even amino acids. Thus, we wondered whether if we were to directly form an amino acidic-peptidic corona around CuS_x nanoclusters (CuS_x NCs), in a bid to greatly increase the uptake of the nanoclusters. If uncoated CuS_x NCs were presented to bacteria, there is no incentive to take up the nanoclusters and any uptake will be stochastic driven. With the amino acidic-peptidic corona, from the perspective of the bacteria, it is chemically like a protein since the nanoclusters are the size of a protein complex [51,52]. We then proposed to use a complex mixture of amino acids and peptides collectively called Amino-Pep arising from tryptic digestion of casein, to form the corona. The amino acidic-peptidic corona greatly enhanced the uptake of copper sulfide nanoclusters whose enhanced therapy of bacteria-infected wounds. These antibacterial agents, based on CuS_x NCs, were developed using a straightforward and environmentally friendly synthesis method and consist of essential components (Scheme 1). Such approach is easy and scalable with no need of high pressure and temperature or special Apparatus. Considering the easily synthesis, scalability and the high abundance elements of Cu and S in life together, such Amino-Pep-CuS_x provided the high potential for catalytic, semi-conducting and biomedical applications. Additionally, for comparison, we have used a full length blood protein of the highest concentration in blood, serum albumin to form the corona of the same CuS_x NCs. The amino acid-peptide corona resulted in 3 orders of magnitude fewer colony-forming units compared to conventional CuS_x NCs modified with serum albumin. The small-sized CuS_x NCs exhibited a broad-spectrum nature and possessed multiple valence states, conferring upon them both photothermal and Fenton-like catalytic properties [41]. This unique combination allowed the NCs to function as a sunlight activated photothermal and chemodynamic nanoagent. Furthermore, the formation of CuS_x NCs incorporated a defect engineering approach by carefully regulating the ratio of copper (Cu) to sulfur (S) elements. The sulfur defect in CuS_x NCs decreased as the element ratio of Cu and S increased. This reduction resulted in an elevation of the photothermal effect under sunlight irradiation, a decrease in catalytic capability against H_2O_2, and an increase in glutathione (GSH) consumption to disrupt cellular antioxidant defense systems through redox reactions. Post-treatment, these NCs, known for their good biocompatibility, can eventually decompose without toxicity to the injury site, ensuring excellent biosafety. It also demonstrated the development of with enhanced bactericidal efficiency, presenting a broader application prospect.

2. Experimental and characterization

2.1. Materials

All chemicals and reagents (analytical grade) were used as received without any further purification. Copper chloride ($CuCl_2$•$2H_2O$), sodium sulfide (Na_2S•$9H_2O$), tryptone (Amino-Pep), bovine serum album (BSA), 3,3′-Diaminobenzidine tetrahydrochloride tablet (DAB), and methylene blue (MB) were all purchased from Sigma-Aldrich Co. (Singapore). The lysogeny broth (LB) medium in all bacterial cultures was pre-treated by autoclaving at 120 °C for 20 min before use. And the water used in the experiments was sterile and enzyme-free if not specified from a Milli-Q system (Health Force Biomeditech Holdings Ltd.).

2.2. Characterization

UV–vis absorption spectra were determined by UV–vis spectrophotometer. Dynamic light scattering (DLS) measurements and zeta potential were performed on the Malvern Nano-ZS Particle Size. The contents of copper ions in those samples were determined by using inductively coupled plasma atomic-emission spectroscopy (ICP-AES, Thermo). The binding energy of the sample were characterized by X-ray photoelectron spectroscopy (XPS; AXIS HIS, Kratos Analytical). The powder XRD measurements were performed using a Bruker D8 advanced diffractometer with a Cu Ka irradiation in the 2θ range of 200–600. PLS-SXE300 (200–2500 nm, 1526 W/m^2) purchased from PerfectLight Co., Ltd. was used for photothermal experiments. IR thermal image was recorded by the photothermal camera FLIR T420. Scanning electron microscope (SEM) images were obtained by field emission SEM (JEOL, JSM-7610FPlus). TEM images were obtained on a JEM 1400 transmission electron microscope with an accelerating voltage from 40 to 120 kV.

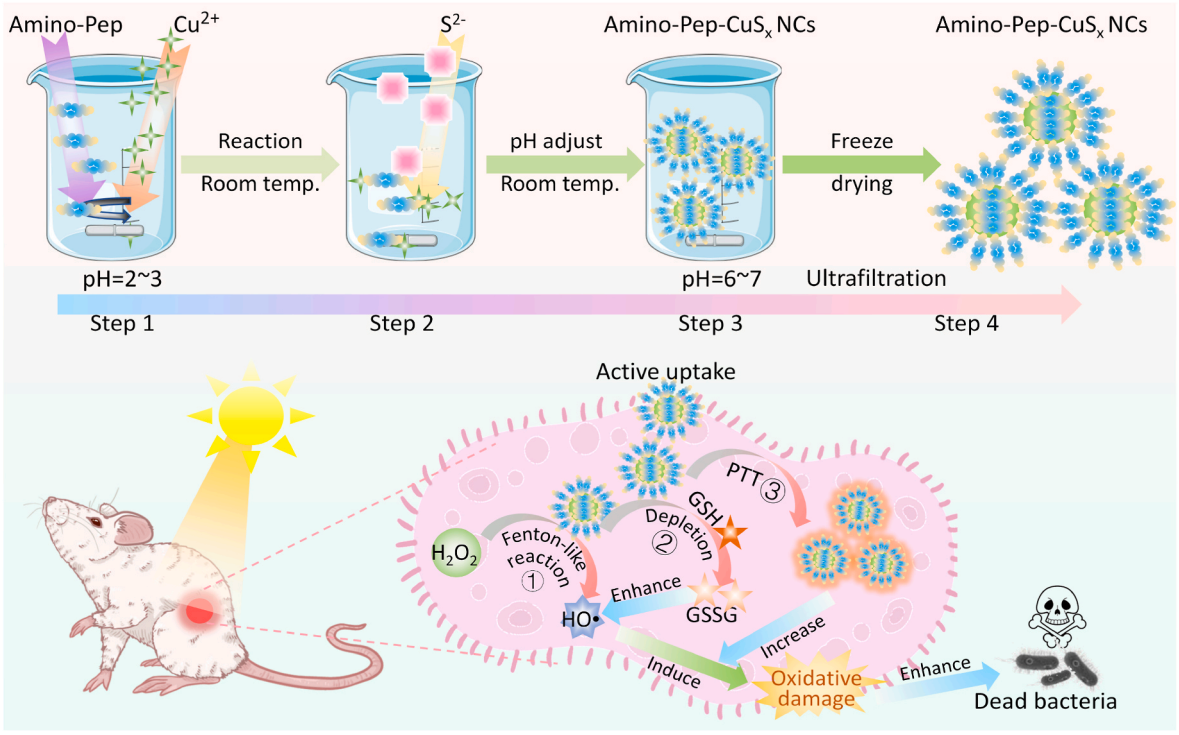

Scheme 1. Schematic illustration of synthesizing bacteria eating Amino-Pep modified CuS_x NCs for enhanced photothermal and chemodynamic anti-bacteria. Step 1: adjusting pH value of mixture solution containing amino-peptides and copper ions; Step 2: mixing solution accompanying with dropwise adding sulfide ions; Step 3: adjusting the pH value of reaction solution to 6–7; Step 4: purifying the final solution with ultrafiltration tube. Synergetic effect including 3 aspects: ① producing toxic HO• through fenton-like reaction between copper and H_2O_2; ② consuming GSH to generate GSSG which restricts redox reactions; ③ photothermal effect from CuS_x NCs to produce heat that increase the above reactions.

2.3. Synthesis of amino-pep and BSA modified CuS_x NCs

In a typical procedure, the Cu-precursor solution was firstly prepared by dispersing 0.5 mL Cu^{2+} solution (0.1 M) and 40 mg amino-Pep/BSA into 40 mL water, and the pH value was adjusted into 2.0–3.0 by 1 M HCl. Then, 0.05, 0.1, 0.2, 0.4 and 0.6 mL S^{2-} (0.5 mol/L) was dropped slowly under vigorous stirring at room temperature, respectively. Add to the mixture, and stir continuously during this process. After adding $Na_2S•9H_2O$, quickly adjust the pH of the solution to neutral. After ultrafiltration with an ultrafiltration centrifuge tube with a retention capacity of 10 KD, the solution was repeatedly washed three times, and finally, the CuS_x NCs concentration was detected using ICP-MS.

2.4. Analysis of ROS from Amino-Pep-CuS_x NCs

3,3′-diaminobenzidine (DAB) and MB were used to indicate ROS generation from Amio-Pep-CuS_x NCs at different pH and temperature conditions. For the DAB assay, DAB solution was mixed with H_2O_2 at pH = 5.0, 6.5 7.4, 9.0 and CuS_x NCs were added and the change in absorbance at 569 nm was immediately detected to observe the fading of DAB. The MB assay was done in 25 mM sodium bicarbonate-CO_2 equilibrium, and the change in absorbance of the mixture at 665 nm after CuS_x addition was observed, which was caused by the generation of a purple/brown product. All experiments were performed at room temperature if not otherwise specified.

2.5. Photothermal measurement of Amino-Pep-CuS_x NCs

The solution temperatures were monitored by using an IR thermal camera. Experiments were taken out in 0.2 mL 1 × PBS solutions (pH = 7.4) containing different concentrations of Amino-Pep-CuSx NCs. When the samples were exposed to a solarlight intensity of 1526 W/m^2, the temperature was recorded every 20 s for 10 min. To explore the photothermal conversion stability of Amino-Pep-CuS_x NCs, its aqueous dispersion (Cu ion concentration of 0.6 mM) was irradiated by solarlight (1526 W/m^2) for 10 min, then the laser was off for 10 min to cool the sample. And 0.1 mM ICG was used to compare the photothermal stability. The on/off irradiation cycle was repeated for five times.

2.6. Bacterial culture

Staphylococcus aureus ATCC 6538 and Escherichia coli ATCC 25922 were inoculated on LB agar plates after shaking overnight at 37 °C and 200 rpm in LB medium and cultured overnight. For each experiment, fresh colonies on the agar plates were selected and LB liquid medium was selected for their expanded culture for approximately 14 h, and the experiment could be started.

2.7. In vitro antibacterial assays

The solution temperatures of bacteria medium incubated with CuS_x NCs were monitored by using an IR thermal camera. 0.6 mM of CuS_x NCs solution was exposed to solar light (200–2500 nm, 1526 W/m^2). The temperature was recorded every 20 s until the temperature reached maximum (10 min). additionally, Dichlorodihydrofluorescein Diacetate (DCFH-DA) was used to detect the amount of ROS produced by CuSx NCs and bacteria. CuS_x NCs, *E. Coli* and DCFH-DA were mixed in LB liquid medium, and exposed to solar light (200–2500 nm, 1526 W/m^2) for 30 min. DCFH-DA is later oxidized by ROS into 2′, 7’ –dichlorofluorescein (DCF). DCF is detected by BioTek Synergy H4 microplate reader with excitation/emission at 485 nm/535 nm before and after solar light exposure. The change of fluorescence was detected to observe the generation of ROS.

CuS_x NCs were mixed with bacteria for a certain period and then centrifuged at 2000 rpm for 15 min. The lower layer of bacteria was mixed with aqua regia overnight, diluted to pH neutral, filtered, and

subjected to ICP-MS experiments. For CuS_x NCs uptake in some mouse organs/tissues, 0.1 mm^3 tissues were taken and mixed with aqua regia overnight, diluted to pH neutral, filtered, and then subjected to ICP-MS experiments.

2.8. Cytotoxicity assay and cellular uptake of Amino-Pep-CuS_x NCs

The cytotoxicity of Amino-Pep-CuS_x NCs at different concentrations and atomic ratios was examined with the help of this experiment. The specific experimental steps: the same number of normal hepatocytes-LO2 were inoculated into 96-well plates and incubated overnight until the cells were completely stretched, then the same volume of CuS_x NCs was added according to the concentration gradient, and after incubation overnight again, 20 μL 3-(4,5-Dimethylthiazol-2-yl)-2,5-diphenyltetrazolium bromide was added. After incubation for 4 h in a cell culture incubator protected from light, the supernatant was aspirated and 200 μL of DMSO was added to each well. And after shaking for 10 min, the absorbance of each well was measured at 490 nm and the results were calculated based on the metric of Cell Viability = OD (sample) - OD (control)/OD (control) × 100 %.

2.9. Animal models of bacterial infection

C57BL/6J mice were used to construct an animal model of bacterial infection. The detailed steps were to use 24C57BL/6J mice at 6–8 weeks of age, cut a circular wound of about 1 cm in diameter into the skin of the back of each mouse with surgical scissors, and completely remove the skin. Approximately 12 h later, a mixture of *S. aureus* ($1.2*10^6$ CFU/mL) and *E. coli* ($1.2*10^6$ CFU/mL) was applied to the open wounds, and after a 2 h interval, the same wounds were repeatedly once with the same bacterial mixture.

2.10. Animal models assay

The model mice were randomly divided equally into 2 large groups, each of which was further divided into 3 groups: control group, Amino-Pep-CuS_x NCs treatment group, and BSA-CuS_x NCs treatment group, which were treated according to the grouping method in Fig. 7A. The Amino-Pep-CuS_x NCs treatment group applied 0.6 mM of Amino-Pep-CuS_x NCs 100 μL to the wounds of mice one day apart; the BSA-CuS_x NCs treatment group applied 0.6 mM of Amino-Pep-CuS_x NCs 100 μL to the wounds of mice one day apart; the control group applied 100 μL saline to the wounds of mice one day apart. Meanwhile, each time, the mice were weighed and the wound diameter, d was measured one day before treatment, and throughout the study. The wound area and the wound healing curve was plotted according to formula $S = \pi d^2/4$. Documenting wound changes was done with a digital camera.

3. Results and discussion

3.1. Fabrication and characterization of Amino-Pep-CuS_x NCs

The medium ingredients for *in vitro* culture of Luria-Bertani bacteria typically include NaCl, yeast extract, and Amino-Pep [53]. To enhance the uptake efficiency of CuS_x NCs, we employed Amino-Pep to encapsulate defected-CuS_x NCs through a straightforward and gentle bottom-up approach [54,55], rendering the NCs a preferred nutritional source for bacteria. This method was initiated by a chemical reaction between Cu^{2+} and $Na_2S{\bullet}9H_2O$, as depicted in Scheme 1, where Amino-Pep also served as a surfactant and stabilizer to control the size of CuS_x NCs. The pH of the Cu^{2+}-Amino-Pep complex solution, formed by Amino-Pep and $CuCl_2{\bullet}xH_2O$, was adjusted to approximately 2–3. A solution containing S^{2-} was then introduced into the above mixture, leading to the formation of stable CuS_x NCs. Initiation of the reaction between CuS_x and oxygen was triggered through regulating the pH value of solution to around 7, causing a gradual change in solution color to brownish-black, indicative of the formation of small-sized defected CuS_mO_{1-m} NCs. To explore defect engineering, CuS_x NCs with varying sulfur defects were synthesized by adjusting the initial feed molar ratios of Cu^{2+} and S^{2-} (2:1, 1:1, 1:2, 1:4, and 1:6 denoted as CuS_x NCs-2, CuS_x NCs-1, CuS_x NCs-0.5, CuS_x NCs-0.25, and CuS_x NCs-0.17). Transmission electron microscopy (TEM) revealed that the primary size of ultra-small CuS_x NCs was in the range of 3–4 nm, demonstrating a consistent size distribution with no noticeable aggregation of NCs (Fig. 1A and Fig. S1). To illustrate the impact of sulfur defects on size, the average hydrodynamic diameters of CuS_x NCs were measured in the range of 10–50 nm by dynamic light scattering (DLS) (Fig. 1B). The sizes exhibited a gradual decrease from 44.8 to 19.1 nm with the molar ratio of Cu to S decreasing from 2 to 0.17. This phenomenon could be attributed to a reduced surface chelation of Amino-Pep on CuS_x NCs. It is noteworthy that these sizes were slightly larger compared to those observed in TEM images due to the contribution of Amino-Pep extended in solution in light scattering measurements and the shrinkage of NCs measured by TEM.

The impact of sulfur defects on the optical properties of CuS_x NCs was explored under physiological conditions. Across varying sulfur defect levels, all CuS_x NCs exhibited prominent absorption peaks around 360 nm, aligning with the excitonic characteristics of CuS_2 NCs. A decrease in sulfur defect in CuS_x NCs resulted in broader absorption spectra, accompanied by a slight increase in absorbance at 320 nm (Fig. 1C). Correspondingly, the integral absorbance area was observed to increase. This negative correlation between optical properties and defects suggested a potential enhancement in the photothermal effect with decreasing sulfur defects. This will benefit to improve the findings of potential nanoagents in future PTT. By leveraging the prominent peak in the UV region, the estimated size of CuS_x NCs was approximately 3.5 nm [54,56], aligning with the measurement obtained by TEM. Applying Tauc's equation, the corresponding bandgap energy of the NCs exhibited a slight decrease from 3.37 to 3.25 eV (Fig. 1D). This slight decrease can be attributed to the presence of sulfur defects and the incorporation of oxygen atoms serving as n-type dopants. The high concentration of oxygen incorporation induced an increase in charge carriers, resulting in bandgap narrowing. It is important to note that the collective influence of surface states and localized defect states can contribute to lowering the determined energy of optical bandgap.

To examine the crystalline structure of CuS_x NCs, X-ray diffraction (XRD) spectra were determined individually for five samples (Fig. 1E). All diffraction peaks and relative intensities at $2\theta = 31.3°$, 45.03°, 56.1°, 64.7°, and 75.0° were observed, matching well with (200), (220), (222), (400), and (420) planes of the pure cubic Cu_2S standard peak (JCPDS, No: 84–1770) [57]. Furthermore, the peaks for CuS_x NCs (−2 and −1) with high defects exhibited broadening with weak peaks, indicating a less crystalline structure. In contrast, distinct diffraction patterns for CuS_x NCs with low sulfur defects were well-identified, showing a highly crystalline structure. This suggests that the degree of crystallinity gradually increased with an increase in sulfur content, indicating uniform defects present across all CuS_x NCs. The surface electronic states and chemical composition of all CuS_x NCs were thoroughly examined using X-ray photoelectron spectroscopy (XPS) [58]. As illustrated in Fig. S2, the XPS survey spectrum of the five CuS_x NCs samples displayed distinct peaks corresponding to Cu, S, O, C, and N elements. In the Cu 2p XPS spectrum (Fig. 1F), the binding energy (B.E.) peaks at 931.9–932.4 eV and 951.7–952.2 eV respectively corresponded to Cu 2p3/2 and Cu 2p1/2, indicating the presence of Cu(I) oxidation state in all samples. Furthermore, the corresponding B.E. peaks at 933.2–934.0 eV and 955.6–956.3 eV for Cu 2p3/2 and Cu 2p1/2 demonstrated the presence of Cu(II) oxidation state. Satellite peaks were also observed at around 947.3–948.0 eV between the binding energies of Cu 2p3/2 and Cu 2p1/2, attributed to Cu(II) in the paramagnetic chemical state. Additionally, with decreasing sulfur defects, a slight shift to higher energy binding was observed in all peaks for Cu 2p, indicating an increase in charge carriers induced by the incorporation of more electronegative

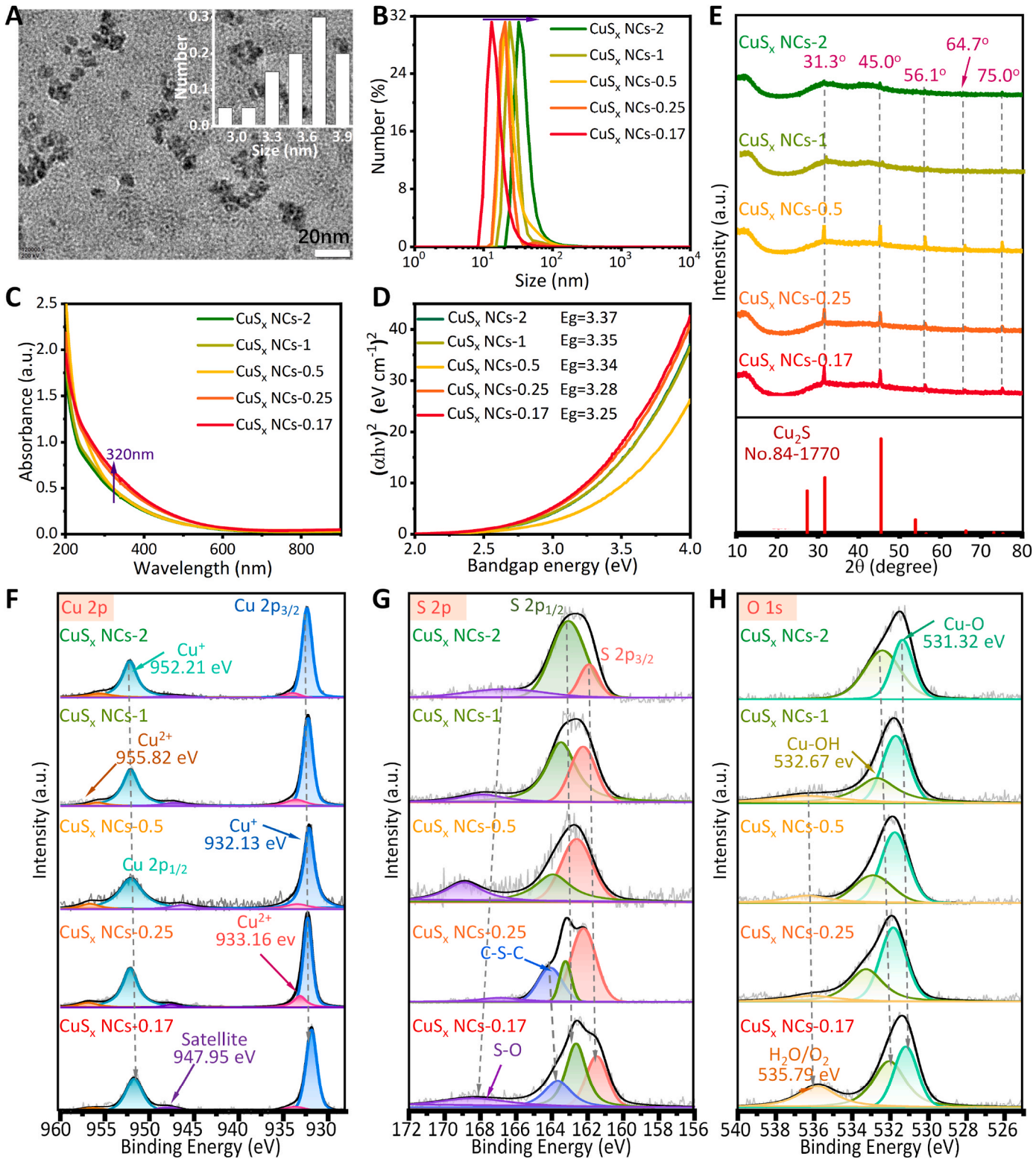

Fig. 1. Characterization of Amino-Pep-CuS_x NCs. **(A)** TEM of CuS_x NCs-1; **(B)** hydrodynamic size; **(C)** UV absorption spectra; **(D)** bandgap energy; **(E)** XRD and **(F-H)** XPS spectrum of CuS_x NCs with different sulfur defects. According to the molar ratio of added Cu to S, the ratios of 2, 1, 0.5, 0.25, and 0.17 can be recorded as CuS_x NCs-2, CuS_x NCs-1, CuS_x NCs-0.5, CuS_x NCs-0.25, and CuS_x NCs-0.17, respectively.

oxygen atoms. A parallel oxidation pattern was noticeable at the S 2p region in the high-resolution XPS spectrum. Sulfur exhibited two distinct chemical states, with representative peaks at around 161.5 eV and 163.0 eV corresponded to S 2p3/2 and S 2p1/2 bands, respectively (Fig. 1G). Additional peaks at around 164.0 eV and 163.1 eV were observed and attributed to the signal of C-S-C bond originating from CuS_x NCs-0.25 and CuS_x NCs-0.17, reflecting a high sulfur content. Larger binding energy peaks (166.6–168.9 eV) in all samples confirmed the presence of an elevated valence sulfide state, suggesting that sulfur appeared to undergo oxidation readily during the chemical reaction

process involved in preparing CuS_x NCs. It is noteworthy that the S-O bond peak position shifted notably towards higher binding energies as the molar ratios of Cu to S decreased. One potential explanation is that an increased substitution of oxygen atoms was along with the higher presence of sulfur vacancies during the in-situ formation of CuS_x NCs. For a more thorough examination of the chemical valence state and its correlation with the oxygen content, Gaussian fitting was employed to deconvolute the O 1s peaks in the XPS spectrum of the five CuS_x NCs samples. (Fig. 1H). The characteristic peaks observed at lower binding energies (around 531.2 eV) were attributed to the Cu-O bond within a stoichiometric CuO_mS_{1-m} structure, while another representative peak at the higher binding energy (~532.7 eV) was assigned to Cu-OH originating from oxygen deficiency in CuS_x NCs. Notably, higher binding energy peaks at around 535.8 eV in CuS_x NCs were associated with absorbed H_2O and O_2. Furthermore, the zeta potential of different defected Amino-Pep-CuS_x NCs aqueous solution was measured to be in the range from −9.84 to −3.16 mV (Fig. S2A), indicating the negatively charged Amino-Pep stabilizer is decorated on the surface of the CuS_x NCs. The surface functional groups on CuS_x NCs were investigated and compared with bare tryptone and BSA through the Fourier transform

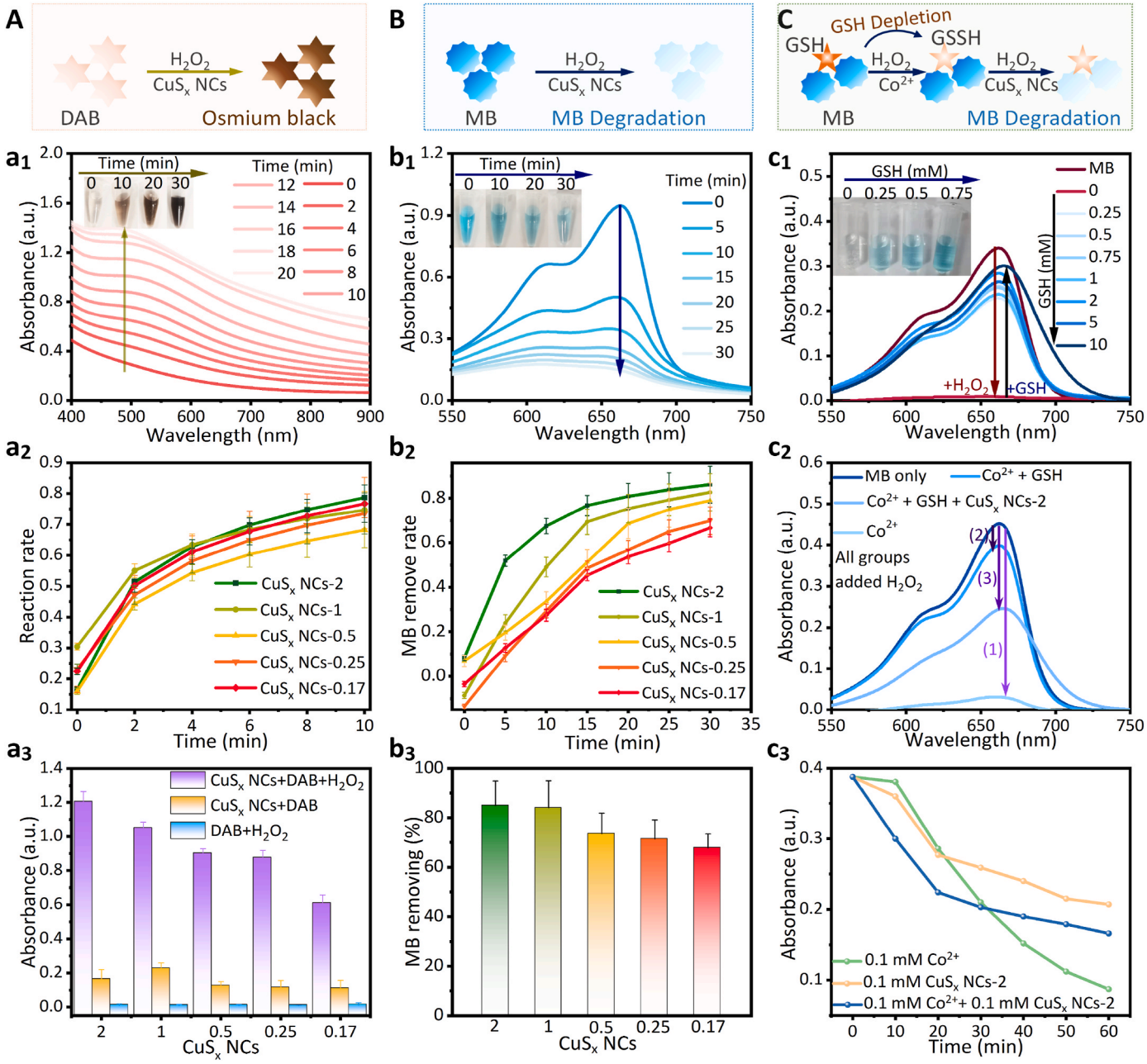

Fig. 2. Catalytic activity of different defected CuS_x NCs through Fenton-like reaction. (**A**) Assessment of HO• generation from CuS_x NCs measured by DAB agent with H_2O_2; (**a1**) UV spectra of DAB solution with CuS_x NCs-2 solution and H_2O_2 for 20 min (inset: solution color change for 30 min), (**a2**) the kinetics of catalytic reactions of DAB with different defected CuS_x NCs and H_2O_2, (**a3**) UV absorbance of DAB incubated with different defected CuS_x NCs and H_2O_2 for 20 min; (**B**) Assay of HO• production from MB degradation incubated with CuS_x NCs and H_2O_2; (**b1**) MB degradation by CuS_x NCs-2 and H_2O_2 for 30 min (inset: solution color change for 30 min), (**b2**) MB degradation kinetics treated with different CuS_x NCs-2 and H_2O_2 for 20 min, (**b3**) MB removing rate by different CuS_x NCs-2; (**C**) GSH depletion by CuS_x NCs-2, [Co^{2+}] = 0.1 mM, [CuS_x NCs] = 0.1 mM, [GSH] = 1 mM; (**c1**) the ability of CuS_x NCs-2 to deplete GSH at different concentrations within 30 min (inset: solution color change of MB with different concentrations of GSH), (**c2**) degradation degree, and (**c3**) MB degradation kinetics with various catalyst components in the presence of H_2O_2.

infrared (FTIR), indicating the components of CuS_x NCs.

3.2. Regulating chemodynamic effect upon defect of CuS_x NCs

To explore the impact of defects on the chemodynamic properties of defect-engineered CuS_x NCs, we employed 3,3′-diaminobenzidine (DAB) as a chromogenic agent to gauge H_2O_2 consumption, indicative of the Fenton reaction rate (Fig. 2A) [59–62]. The UV spectrum of DAB exhibited a significant increase within the initial 10-min upon the introduction of various defect-engineered CuS_x NCs and H_2O_2 (Fig. 2A1 and Fig. S3), leading to a color transformation in the solution from light brown to dark brown (Fig. 2A inset). Evaluating the catalytic rates of different CuS_x NCs through monitoring the absorbance change at 569 nm revealed that samples with higher sulfur defects initially exhibited enhanced catalytic activity. However, as time progressed, the catalytic rate decelerated, eventually manifesting a diminished catalytic degree over minutes. This trend pointed towards a notable connection between catalytic rate, reaction duration, and sulfur levels in the bio-catalysts, as observed in Fig. 2A2. Considering the relatively extended duration of the chemodynamic effect (CDT) treatment, we standardized the amounts of generated radicals at 10 min for a comparative analysis, as depicted in Fig. 2A3. Evidently, the absorbance at 569 nm of DAB gradually decreased with an increase in sulfur content in CuS_x NCs. These observations strongly suggested a positive correlation between the generation of HO• from CuS_x NCs and sulfur defects, collectively indicating the favorable impact of defects on Fenton-like catalytic activity. Importantly, it's worth noting that no discernible influence was found in the control groups. Also, the influence of Ph values on catalytic rates of CuS_x NCs-2 were evaluated using DAB in PBS at pH5.0, 7.4 and 9.0 (Fig. S4). It's clearly shown that acidic condition can facilitate the Fenton-reaction rate, induced more HO• to faster bacteria apoptosis. This will be benefit for promoting wound healing due to the acidic environment of inflamed and infectious wound.

To further identify and compare the Fenton activity of defect-engineered CuS_x NCs, methylene blue (MB) was utilized for detecting the generation of HO•. It was evident in Fig. 2B1 (Fig. S5) that MB was rapidly degraded within 30 min in the presence of defect-engineered CuS_x NCs and H_2O_2, indicating the generation of ROS. Besides this, a correlation was observed between the degradation rates of MB and increasing Cu/S ratios. Notably, among the six groups, samples with higher sulfur content displayed a better catalytic activity at the first short time, then the catalytic rate slowed down and finally exhibited lower catalytic degree on a timescale of minutes, revealing that the catalytic rate was strongly related to reaction time and sulfur level in catalysts, CuS_x NCs-2 exhibited superior degradation capability, with a kinetic rate constant of approximately 0.065 (min^{-1}) within the initial 10 min. As illustrated in Fig. 2B2, the impact on MB absorbance was negligible when CuS_x NCs or H_2O_2 were applied individually. However, upon combining CuS_x NCs-2, 1, 0.5, 0.25, and 0.17 with H_2O_2, the degradation efficiency of MB gradually decreased from 84.9 %, 84 %, 73.5 %, 71.4 %, to 67.8 %, as depicted in Fig. 2B3. Evidently, the superior catalytic performance of the NCs-2 and 1 group are manifested by a higher degradation rate of MB within 20 min. This outcome suggests an augmented generation of radicals resulting from the interaction between CuS_x NCs and H_2O_2, facilitated by the enhanced sulfur defect. This observation aligns with previous findings using the DAB probe.

Collectively, the data clearly indicates that defect engineering in the synthesized CuS_x NCs significantly enhances Fenton-like catalytic efficiency. Additionally, we explored the impact of GSH on the degradation of MB induced by HO• and assessed the process of GSH depletion by CuS_x NCs, as illustrated in Fig. 2C. Examining Fig. 2C1, it is evident that the scavenging efficiency of CuS_x NCs-2 on MB reached nearly 90 % after 30 min in the absence of GSH. However, the presence of added GSH impeded the scavenging process, causing the efficiency of CuS_x NCs to decrease to 13.2 % as the GSH concentration increased to 10 mM. This observation underscores the ability of GSH to eliminate ROS. To delve deeper into the improved chemodynamic efficacy resulting from GSH depletion, we introduced the exogenous HO• -generating catalyst Co^{2+}, well-documented as a Fenton-like catalyst for radical generation from H_2O_2 (Fig. 2C2). In the presence of Co^{2+} and H_2O_2, MB degradation reached 93.1 %, but the process was effectively restrained with a degradation efficiency of 11.9 % upon the addition of GSH. Specifically, the intricate equilibrium between the Fenton-like reaction and GSH depletion was disrupted upon the addition of CuS_x NCs into the reaction system. This disturbance resulted in the degradation of MB to 45.6 % after a 3-h incubation period. This observation underscores the significant role played by CuS_x NCs in the GSH depletion process. Furthermore, the Fenton-like catalytic capability of CuS_x NCs was compared with that of the Co^{2+} catalyst (Fig. 2C3). It is evident that the degradation rate of MB was higher after 1 h of incubation with only Co^{2+}/H_2O_2 compared to only CuS_x NCs/H_2O_2, highlighting the relatively weaker catalytic ability of our CuS_x NCs. This observation supports the sequential catalytic activity of CuS_x NCs, which involves GSH depletion through the transition in chemical valence between Cu^{2+} and Cu^{+} in this redox reaction: $Cu^{2+} - CuS_x\ NCs + GSH \rightarrow Cu^{+} - CuS_x\ NCs + GSSG$. CuS_x NCs facilitate the oxidation of GSH to GSSG, leading to GSH depletion and the disturbance of redox homeostasis in the organism. These promising results showcase the heightened chemodynamic activity of CuS_x NCs, indicating their potential for effective deployment through inducing CDT against bacteria.

3.3. Solar light induced photothermal effect of Amino-Pep-CuS_x NCs

The creation of nanomaterials exhibiting high photothermal conversion efficiency under sunlight irradiation conditions is exceptionally appealing, not only for the conservation of fossil energy but also for expanding the range of applications for the material itself [63–65]. Inspired by the broad absorbance across the wavelength range of 200–900 nm, we postulated that CuS_x NCs would manifest a notable solar light-induced photothermal effect [66]. Furthermore, we anticipated a potential detrimental impact of sulfur defects in CuS_x NCs on the photothermal effect (Fig. 3A). To validate this hypothesis, we examined the photothermal properties of CuS_x NCs with varying sulfur defects under solar light irradiation (200–2500 nm, 1526 W/m^2). As depicted in Fig. 3B, the solution temperature of CuS_x NCs-2 to 0.17, at a concentration of 0.6 mM, increased by more than 10 °C and reached from 40.5 to 45.0 after 10-min of solar light exposure. These temperature elevations were respectively 1.35-fold–1.49-fold higher than that observed for PBS (30.1 °C) and exceeded the critical temperature (42 °C) threshold necessary to trigger apoptosis in cancer cells. Noteworthy, it was observed that defect-dependent temperature reductions occurred for all CuS_x NCs. The maximum temperature of CuS_x NCs after 10-min of solar light irradiation increased as sulfur defects decreased potentially linked to the absorption change induced by defects. To visually showcase the outstanding photothermal conversion capability of all CuS_x NCs, corresponding infrared thermal images were monitored. These images revealed a notable contrast in intensity relative to the solution temperature, with the contrast increasing as the defect content in CuS_x NCs decreased and the irradiation duration increased (Fig. 3C). Moreover, ensuring photothermal stability is a fundamental requirement for effective photothermal nanoagents. The temperature variations of all CuS_x NCs dispersions (1.0 mM) were tracked across multiple cycles of irradiation. Impressively, even after undergoing five consecutive heating-cooling cycles, the peak temperatures of CuS_x NCs consistently remained at an elevated level. In contrast, Indocyanine green (ICG) as a NIR photothermal agent, that is commercially available and FDA-approved for clinical use, experienced significant degradation over the same number of irradiation cycles (Fig. 3D). The exceptional photothermal properties and stability demonstrated by CuS_x NCs underscore their potential for applications in photothermal anti-bacteria.

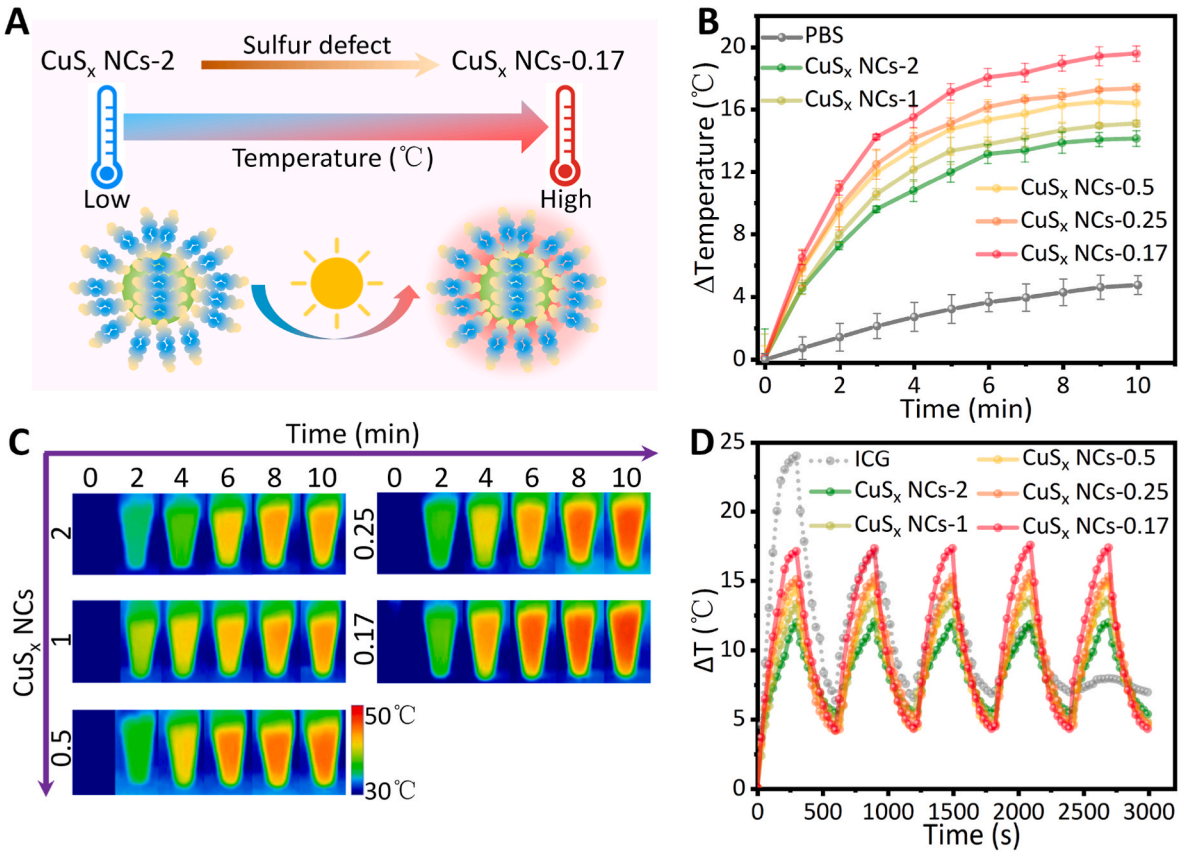

Fig. 3. Solar light induced photothermal effect of CuS_x NCs with different defect degrees. (**A**) Schematic mechanism showing correlation between photothemal effect and sulfur defects; Temperature elevation (**B**) and IR thermal images (**C**) of CuS_x NCs solution with varying molar ratios of Cu and S all at a consistent concentration of 0.6 mM exposed to sunlight irradiation (1526 W/m^2) for 10 min; (**D**) Photothermal stability study of different CuS_x NCs solution (0.6 mM) and control ICG (0.1 mM) experiencing cycles of photothermal heating and natural cooling under solar light irradiation (1526 W/m^2), [CuS_x NCs] = 0.6 mM.

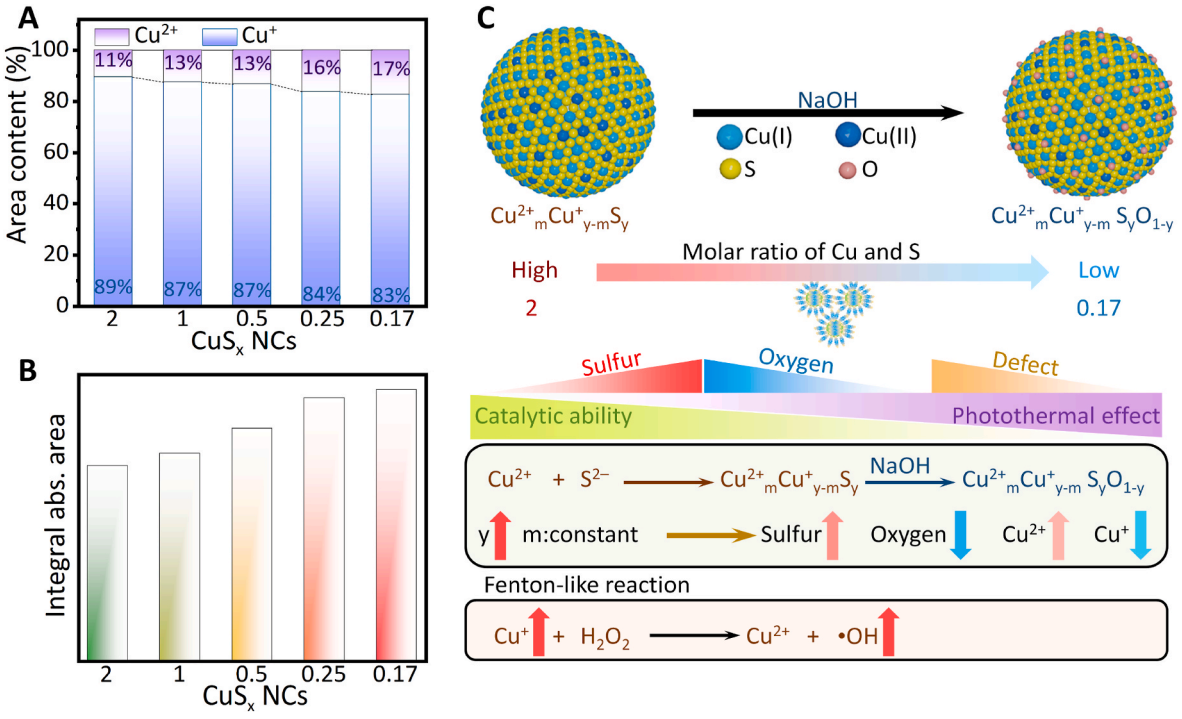

Fig. 4. The relative correlation between photothermal effect, catalytic activity and sulfur defects in CuS_x NCs. (**A**) Area content of Cu^{2+} and Cu^{+} obtained from Cu 2p XPS spectra; (**B**) Integral absorbance area from UV spectra of CuS_x NCs; (**C**) Schematic illustration for mechanism of defect associated photothermal and chemodynamic effect.

3.4. Sulfur defect associated ROS and heat generation

The mechanism underlying the use of defect-engineered CuS_x NCs to regulate photothermal-enhanced CDT was further substantiated by exploring the impact of alterations in the copper valence state, as illustrated in Fig. 4A and B. As the initial ratios of molarity declined from 2 to 0.17, the cupric (Cu^{2+}) level gradually elevated to 17 %, concomitant with a substantial augmentation of the absorption area spanning from 200 to 900 nm. This phenomenon may be ascribed to the elevated concentration of Cu^{2+} within NCs, which could lead to a reduction in bandgap width, thereby inducing widened absorption and ultimately improving the solar light-induced photothermal effect. Nevertheless, the Fenton-like catalytic activity increased with an increase in sulfur defects within 30 min and decreased with a higher amount of Cu^{2+}. This may be attributed to the fact that higher defects induce more active sites, facilitating radical generation, while Cu^{2+} accelerates the consumption of active sites, leading to a reduction in radical generation. Thus, it appears that copper valence significantly influences synergistic PTT/CDT. Based on the above data, the mechanism of defect-engineered CuS_x NCs for Fenton-like process enhanced by photothermal effect can be elucidated as outlined below and depicted in Equations (1)–(3): HO• is produced from H_2O_2 by the oxidation of Cu^{+} [Eq. (1)]. Subsequently, Cu^{2+} is reduced to Cu^{+} by H_2O_2, along with the generation of O_2 and $2H^{+}$ [Eq. (2)]. Concurrently, the sulfur defect may catalyze the

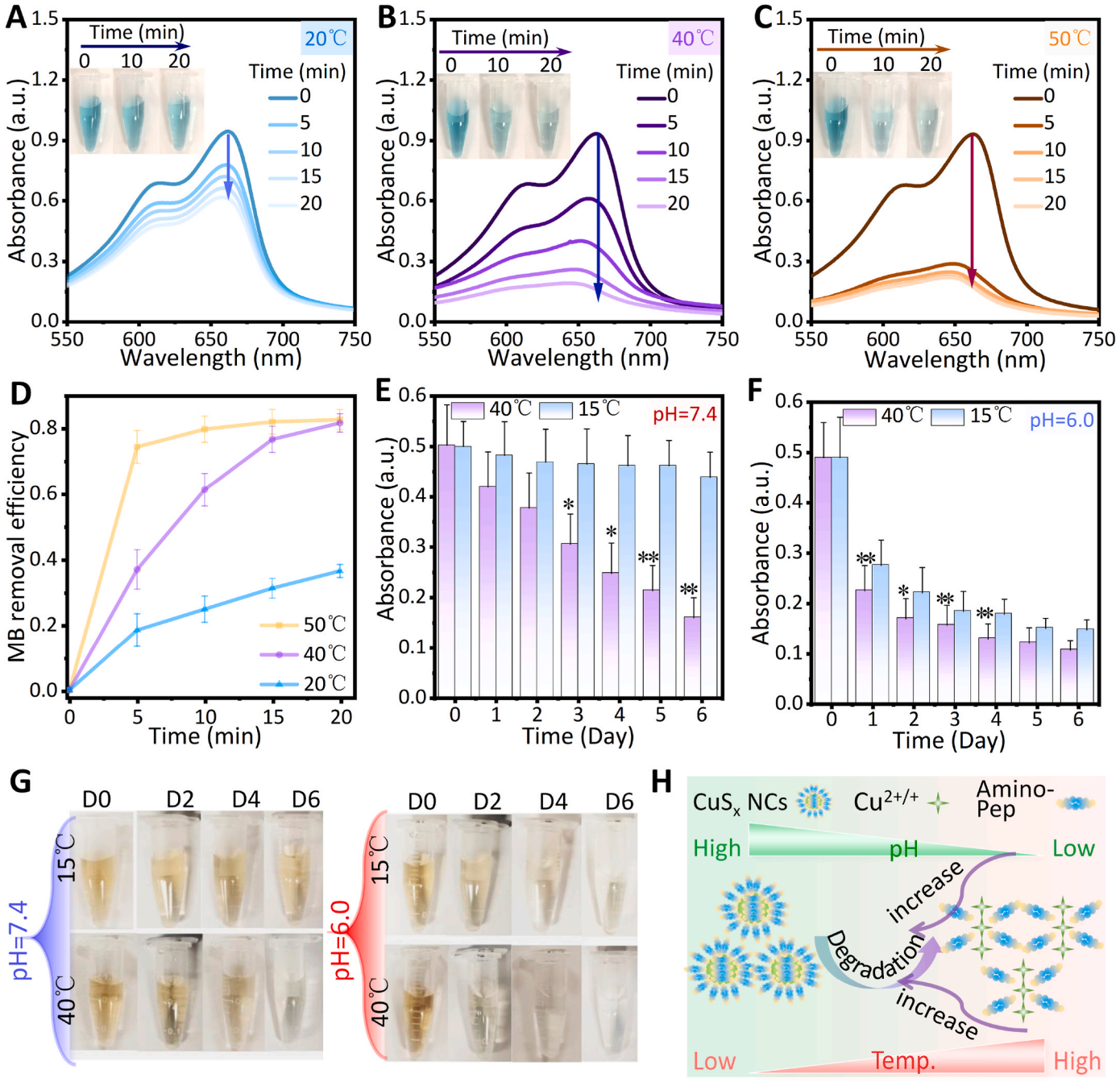

Fig. 5. Thermal-enhanced catalytic activity, thermal and pH amplified degradability of CuS_x NCs-2. Degradation of MB by HO• from CuS_x NCs-2 with H_2O_2 incubated at 20 °C (**A**), 40 °C (**B**), 50 °C (**C**) and (**D**) the comparison of MB removal efficiency; absorbance change of CuS_x NCs-2 at 40 °C and 15 °C incubated for 6 days at pH 7.4 (**E**) and pH 6.0 (**F**); (**G**) The corresponding solution color change of (E) and (F); (**H**) Schematic diagraph of pH and temperature enhanced CuS_x NCs-2 degradation. Data are presented as mean values ± SD (*means $p < 0.05$, **means $p < 0.01$, $n = 3$).

reduction of bound O_2 to O_2^- [Eq. (3)]. CuS_x NCs-2 exhibited the most sustained ROS production, likely due to a higher concentration of sulfur vacancy defects and a higher Cu^+/Cu^{2+} ratio. With increasing sulfur content, the extent of the Fenton-like reaction diminishes because of the restricted sulfur defect concentration.

$$H_2O_2 + Cu^+ \rightarrow Cu^{2+} + HO\bullet + OH^- \quad (1)$$

$$H_2O_2 + Cu^{2+} \rightarrow Cu^+ + O_2 + 2H^+ \quad (2)$$

$$O_2 + e^- \text{(defect)} \rightarrow O_2^- \quad (3)$$

Conclusively, the ratio of Cu^+/Cu^{2+} valence states and sulfur defect levels can jointly regulate total ROS production from the Fenton-like reaction and heat generation from the photothermal effect (Fig. 4C), affirming the potential for tunable hyperthermia-enhanced CDT through defect engineering of CuS_x NCs.

3.5. Heat accelerated CuS_x NCs driven catalysis and its degradation

In light of the results, it is evident that the photothermal and chemodynamic properties of CuS_x NCs exhibited a noteworthy dependence on the amount of sulfur present. Notably, the sulfur-deficient configuration of CuS_x NCs enhances the Fenton-like reaction while diminishing the photothermal effect. Among these samples, those CuS_x NCs-2 samples demonstrated the highest ROS generation, coupled with a simultaneous and considerable increase in temperature. Hence, CuS_x NCs-2 samples were selected for the following experiments due to the potential superior therapy performance resulting from the synergistic chemodynamic and photothermal effect. Building upon these, the investigation focused on the thermally improved Fenton-like process, utilizing MB as a ROS indicator under three distinct temperature regimes (Fig. 5A, B, and **C**). The UV spectra of MB exhibited a consistent decline after a 20-min incubation with CuS_x NCs-2 and H_2O_2 at temperatures of 20 °C, 40 °C, and 50 °C. Concurrently, the color of the MB solution faded within the same time frame. Noteworthy is the observation that the absorption and color reduction occurred at a quicker rate with increasing temperature, indicating a temperature-dependent impact on the process. During the initial 5-min incubation with CuS_x NCs-2/H_2O_2, the rate of MB degradation at 50 °C was observed to be 0.149, surpassing that at 40 °C and 20 °C by 2.02- and 4.05-times, respectively. This underscores the temperature-dependent acceleration of the Fenton-like reaction, as depicted in Fig. 5D. Simultaneously, after 20-min incubation, the MB removal efficiency at 50 °C and 40 °C both peaked at 82.7 % and 81.7 %, respectively. These values were about 2.27- and 2.24-times higher than the efficiency observed at 20 °C, demonstrating the temperature-enhanced efficacy of the process. This result suggested that increased heat could enhance the ROS generation from Fenton-like reaction, in turn, positively influencing the chemodynamic effect. While numerous inorganic nanoparticles have demonstrated remarkable performance in the realm of nanomedicine, their clinical translation is notably challenging. This difficulty arises from their prolonged distribution within the body and the potential toxicity that accompanies the generation of ROS when exposed to cellular environments. Notably, bacteria like *E. coli* and *S. aureus* can induce various metabolites during their catabolism and anabolism, resulting in a persistent weak acidic environment enveloped within the bacterial colonies with a pH of approximately 6.

Apart from that, the biodegradation of nanoparticles is a critical consideration to safeguard normal cells from permanent and unnecessary harm. Building on this, the impact of pH value and temperature on the degradation of CuS_x NCs was further investigated by monitoring UV absorption. As depicted in Fig. 5E, when incubated in a neutral aqueous environment (pH = 7.4), the absorbance at 320 nm of CuS_x NCs-2 gradually decreased over a 6-day period at 40 °C, while at 15 °C, it remained almost unchanged. This suggests that hyperthermia accelerates the self-degradation of CuS_x NCs. at a solution pH of 6.0, the absorbance at both 40 °C and 15 °C experienced a rapid decline within a short incubation time, with the absorbance at 40 °C being consistently lower than that at 15 °C (Fig. 5F). Simultaneously, the solution color of CuS_x NCs-2 transitioned from dark brown to pale, and eventually to almost colorless. This color change signified the gradual release of copper ions into the aqueous solution, a result of the auto-degradation of CuS_x NCs, as illustrated in Fig. 5G. Notably, the efficiency at 40 °C and 15 °C over a 6-day period under acidic conditions was 1.15-time and 5.73-time higher, respectively, than that under neutral conditions. These findings highlighted that both elevated temperature and reduced pH values could expedite the degradation process. This accelerated degradation of CuS_x NCs was advantageous in bacteria-infected wounds, leading to reduce *in vivo* accumulation and minimize systemic side effects, as depicted in Fig. 5H.

3.6. Bacteria actively uptake Amino-Pep-CuS_x NCs for enhanced antibacterial effect

In the process of wound healing, inflammation and infection often occur concurrently, potentially hindering the optimal progress of the healing process. Bacterial infection remains a significant challenge in wound healing as it frequently leads to severe complications and is often difficult to completely eradicate. Hence, selecting an exceptional antibacterial agent with the ability to prevent or weaken bacterial activity is of paramount importance. Given that Amino-Pep serves as a primary nutrient source for bacteria in the medium, including *S. aureus* and *E. coli*, it was hypothesized that Amino-Pep-conjugated CuS_x NCs could mimic these "foods." This mimicry is proposed to enhance rapid sterilization through a pathway involving active ingestion by bacteria, as illustrated schematically in Fig. 6A. To assess the potent antibacterial effectiveness of Amino-Pep-CuS_x NCs, *S. aureus* and *E. coli* were selected as model microorganisms for an *in vitro* assessment of antibacterial activity. The images of corresponding colonies and the bacterial viability under different conditions are shown in Fig. 6B and **C**, respectively. Observationally, there is a noticeable reduction in colony numbers with an increase in the sulfur defect of incubated Amino-Pep-CuS_x NCs in the absence of light. The bacterial fatality rate exhibited a decline from 68.8 % to 42.0 % as the Cu/S ratio decreased from 2 to 0.17. This suggests that the defects in CuS_x NCs indeed contributed to the observed antibacterial effect. This observation appears to support the overarching concept that CuS_x NCs with high defects facilitate the generation of HO•, leading to improved bactericidal effects attributed to their elevated Fenton-like activity. Surprisingly, the survival rates exhibited no or minimal decrease for the control and the addition of Cu^{2+}, attributable to their lack of significant Fenton-like activity. Under solar light irradiation, a similar observation was noted, wherein there was a significant decrease in colony numbers as the defect levels increased. In comparison to conditions without irradiation, the light-induced fatality rate of bacteria by CuS_x NCs was respectively 1.23, 1.12, 1.41, 1.35, and 1.59-time higher, suggesting that heat could enhance the antimicrobial efficacy. The intracellular ROS generation ability of Amino-Pep-CuS_x NCs was examined by quantifying the fluorescence levels using reagent DCFH-DA, as shown in Fig. S6A. It was clearly observed that fluorescence of bacteria incubated with BSA-CuS_x NCs and Amino-Pep-CuS_x NCs both increased a little without light irradiation due to chemodynamic effect, while they both increased greatly after light irradiation. In comparison with the control, the fluorescence respectively enhanced by 1.24- and 1.89-time for BSA-CuS_x NCs and Amino-Pep-CuS_x NCs. This phenomenon was due to the fact that HO• generation from the Fenton-like reaction was improved by the light-activated photothermal effect, thereby heightening the antibacterial effect. Contrastingly, the blank control and Cu^{2+} also exhibited antibacterial effects, with bacterial viability as low as 12.1 % and 27.1 %, respectively, under the same conditions.

To validate the role of bacterial active ingestion in the robust bactericidal effectiveness of Amino-Pep-CuS_x NCs, we opted evaluate

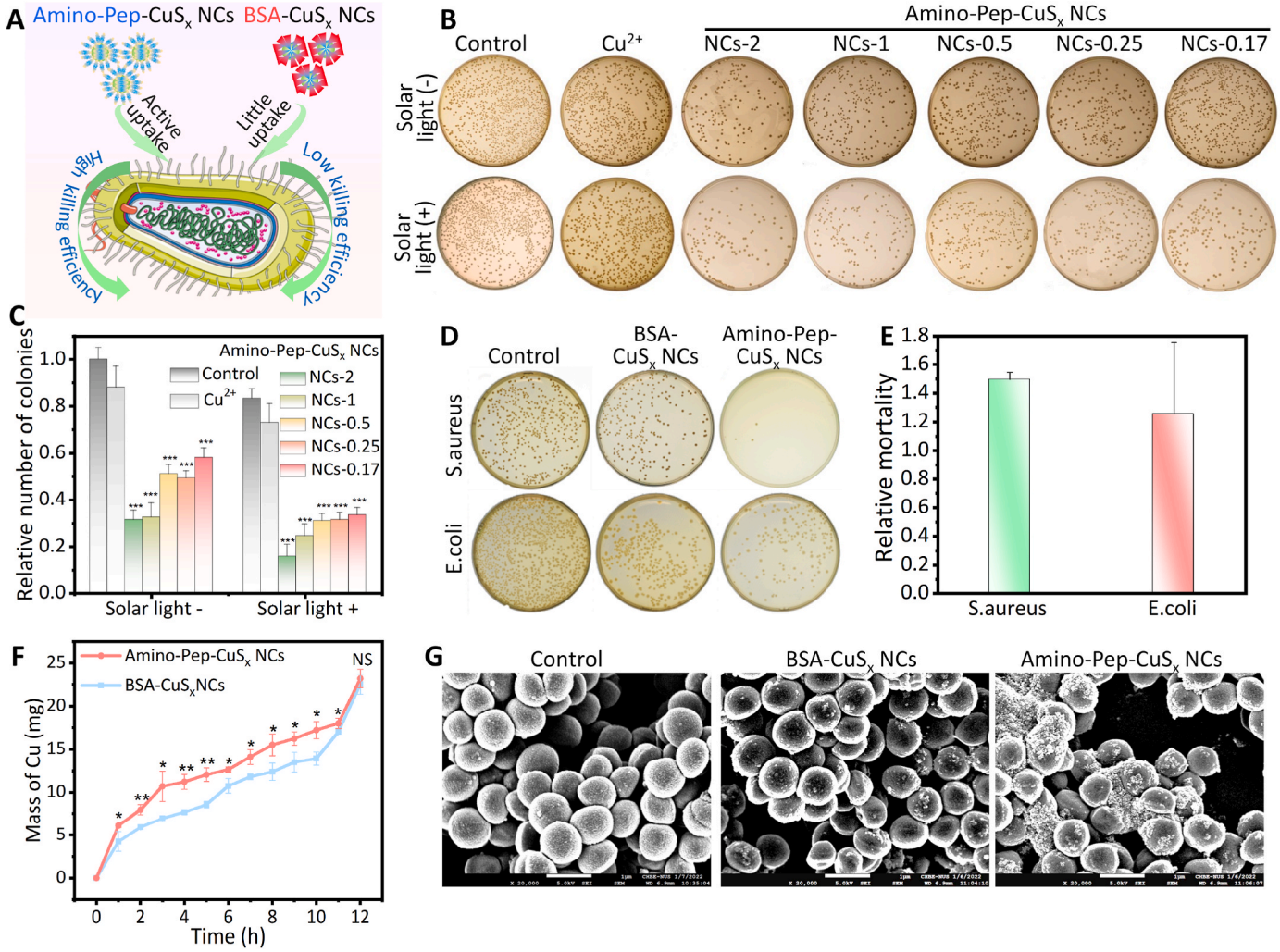

Fig. 6. Bacteria actively eating Amino-Pep-CuS_x NCs for enhanced antibacterial efficacy. (**A**) Schematic showing bacteria eating Amino-Pep-CuS_x NCs for rapid sterilization; (**B**) Photographs of agar plates ([CuS_x NCs] = 0.6 mM) and (**C**) Histograms depicting bacterial counts for S. aureus treated with PBS, Cu^{2+} and different Amino-Pep-CuS_x NCs with and without simulated sunlight irradiation (1526 W/m^2) ([CuS_x NCs] = 1 mM); (**D**) Photographs of agar plates and (**E**) corresponding histograms of bacterial amounts ratio of Amino-Pep-CuS_x NCs-2 and BSA-CuS_x NCs against *S. aureus* and *E.coli* ([CuS_x NCs] = 1 mM); (**F**) Cu mass from the phagocytosis of Amino-Pep-CuS_x NCs and BSA-CuS_x NCs uptake by *S.aureus* using ICP-MS; (**G**) SEM images of PBS, Amino-Pep-CuS_x NCs and BSA-CuS_x NCs treated *S. aureus* after light irradiation, scale bars: 200 nm. The concentration of bacterial cells is approximately 1.0×10^7 CFU. One-way ANOVA analysis was employed for statistical analysis. The error bars indicate the standard deviation calculated from three independent measurements. Data are presented as mean values ± SD (*means $p < 0.05$, **means $p < 0.01$, *** means $p < 0.001$, NS means no significance, n = 3).

the antibacterial effectiveness of BSA-CuS_x NCs on both *E. coli* and *S. aureus* as a comparative analysis (Fig. 6D and **E**). Certainly, despite the observable reduction in bacterial count with BSA-CuS_x NCs with and without light irradiation, attributed to the chemodynamic effect and photothermal-enhanced HO• production, Amino-Pep-CuS_x NCs demonstrated a notable enhancement in antibacterial efficacy. Specifically, Amino-Pep-CuS_x NCs exhibited a 1.50-fold increase against *S. aureus* and a 1.26-fold increase against *E. coli* compared to BSA-CuS_x NCs. This discovery underscored the essential role of actively swallowing in the antibacterial efficacy of Amino-Pep-CuS_x NCs. To provide additional evidence of increased uptake of Amino-Pep-CuS_x NCs by bacteria, we conducted an inductive assessment of the phagocytosis of both Amino-Pep-CuS_x NCs and BSA-CuS_x NCs using Coupled Plasma Mass Spectrometry (ICP-MS) (Fig. 6F and Fig. S7). Clear observations revealed a pronounced superiority in bacterial phagocytosis of Amino-Pep-CuS_x NCs compared to BSA-CuS_x NCs, notably extending up to 12 h. Towards the final time point, bacterial phagocytosis of both CuS_x NCs appeared nearly equal, potentially suggesting saturation where the maximum level of bacterial phagocytosis had been attained. Furthermore, the zeta potential of *E.coli* solution, BSA-CuS_x NCs mixed E.coli solution and Amino-Pep-CuS_x NCs mixed *E.coli* solution were found to change from −11.47, −12.13 and −13.53 mV to −10.72, −11.93 and −10.9 mV after incubation for 4 h, respectively. Obviously, the potential of Amino-Pep-CuS_x NCs incubated *E.coli* decreased the most and to be same with only *E.coli*. This indicated that Amino-Pep-CuS_x NCs was more digested into by bacteria than that of BSA-CuS_x NCs, leading to the similar surface charge property with *E.coli* (Fig. S6B). These outcomes strongly imply a more potent phagocytic effect as Amino-Pep-CuS_x NCs were perceived as a more favorable "food" source by bacteria.

Scanning electron microscopy (SEM) was utilized to elucidate alterations in morphology of bacteria and assess changes in cell membrane integrity. As depicted in Fig. 6G and Fig. S7 and *S. aureus* and *E. coli* bacteria treated with both Amino-Pep-CuS_x NCs and BSA-CuS_x NCs were fragmented into debris upon light irradiation, making it challenge to identify intact bacteria. In contrast, *S. aureus* and *E. coli* subjected to PBS treatment retained their original shape. This phenomenon was attributed to the enhanced Fenton-like activity facilitated by the

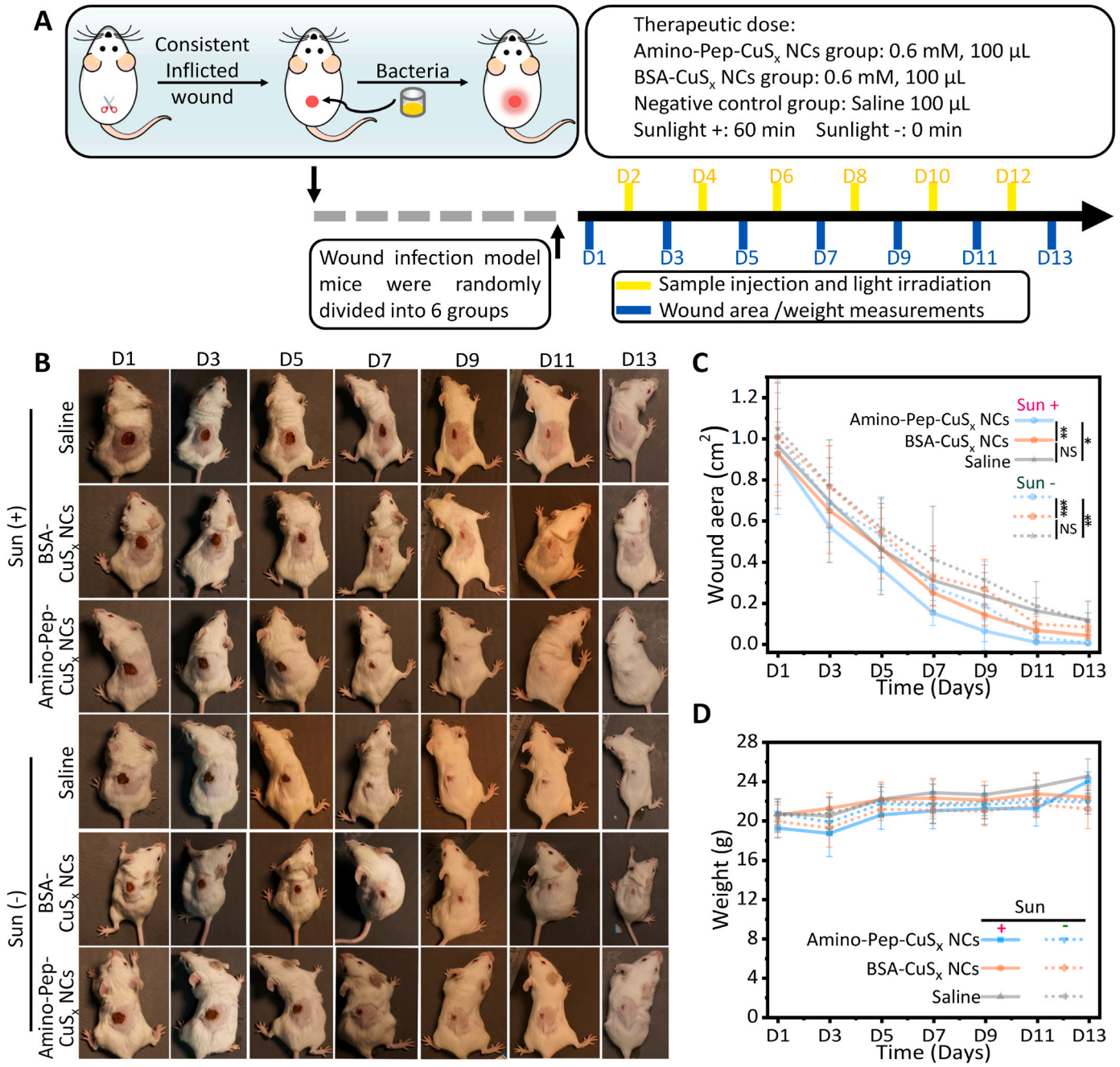

Fig. 7. *In vivo* resistance to bacterial infection of Amino-Pep-CuS_x NCs. (**A**) scheme for constructing an animal model on C57BL/6J mice of bacterial infection by Amino-Pep-CuS_x NCs; (**B**) Photographs depicting the area of the infected wounds in mice during treatment with Amino-Pep-CuS_x NCs; (**C**) Infected area change during Amino-Pep-CuS_x NCs treatment for 13 days. In detail, the solid line segments indicate the sunlight-irradiated components, and the dashed line segments indicate the components without sunlight irradiation; the blue line indicates the Amino-Pep-CuS_x NCs group, the orange line segment indicates the BSA-CuS_x NCs group, and the grey line indicates the saline control group; (**D**) Changes in the body weight of the mice throughout the course of therapy ([CuS_x NCs] = 0.6 mM). Data are presented as mean values ± SD (*means $p < 0.05$, **means $p < 0.01$, *** means $p < 0.001$, NS means no significance, n = 3).

photothermal effect, leading to the oxidation of membrane proteins and peptidoglycan in bacteria [51,67–69]. Specifically, the observed bacterial fragmentation can be ascribed to the destruction of peptidoglycan, a structural component of the cell wall, highlighting its crucial role in maintaining bacterial integrity. Additionally, SEM analysis revealed more pronounced membrane disruption and cytosol condensation in bacteria treated with Amino-Pep-CuS_x NCs compared to those treated with BSA-CuS_x NCs. These observations collectively contribute to the heightened antibacterial activity of Amino-Pep-CuS_x NCs. These results indicated the synergistic bactericidal action and heightened bacterial phagocytosis rate of Amino-Pep-CuS_x NCs, owing to four key factors: the photothermal effect, chemodynamic performance, hyperthermia-accelerated Fenton-like activity, and high uptake enhancement arising from the amino-pep corona.

3.7. *In vivo resistance to bacterial infection*

The cytotoxicity and biocompatibility of Amino-Pep-CuS_x NCs were compared to BSA-CuS_x NCs in their interaction with Human normal colonic epithelial cells (NCM460). The evaluation, depicted in Fig. S8, demonstrated that the cellular activity of NCs remained at approximately 80 % when the concentration was below 0.6 mM. This

observation suggests that a concentration of 0.6 mM is optimal for subsequent anti-infection applications, striking a balance between effectiveness and low toxicity. The *in vivo* antibacterial efficacy of Amino-Pep-CuS_x NCs was examined using a mouse peritonitis-sepsis infection model. Mice were infected with colistin-resistant *E.coli/S. aureus* strains obtained from clinical isolates *via* intra-peritoneal injection. Subsequently, samples, including Amino-Pep-CuS_x NCs, BSA-CuS_x NCs, and saline, were topically applied to the bacteria-infected wounds every two days. At 12-1 pm, direct sunlight exposure for 2 h was intermittently administered to treat the wounds on days 2, 4, 6, 8, 10, and 12. This approach ensured sufficient elevation of temperature above 42 °C, activating the photothermal effect as illustrated in Fig. 7A. Following the administration of various therapies, the wound healing progress in mice was observed for 13 days during the follow-up observations. Substantial reductions in the infected cut areas were observed, indicating significant signs of improvement after the treatments. Observations (Fig. 7B and C) revealed that the wound areas in mice treated with Amino-Pep-CuS_x NCs, both with and without sunlight irradiation, were completely healed after the 6th treatment. In contrast, for those treated with BSA-CuS_x NCs, the healing rates were 96.3 % and 92.2 %, respectively, demonstrating a relatively lower rate of healing. This suggests that the actively swallowing effect of Amino-Pep-CuS_x NCs, coupled with their higher healing efficiency, enhances bactericidal efficacy, aligning with the *in vitro* findings. In addition, following the third treatment, infected wounds treated with Amino-Pep-CuS_x NCs and BSA-CuS_x NCs demonstrated a 13 % and 12 % increase in healing efficiency, respectively, when exposed to sunlight in comparison with those without sunlight exposure. These results signify that the photothermal effect significantly contributed to the enhanced bacterial infection ability of CuS_x NCs. Importantly, both the treatment and control groups exhibited no notable changes in body weight observed throughout the treatment period (Fig. 7D), indicating the favorable biocompatibility of

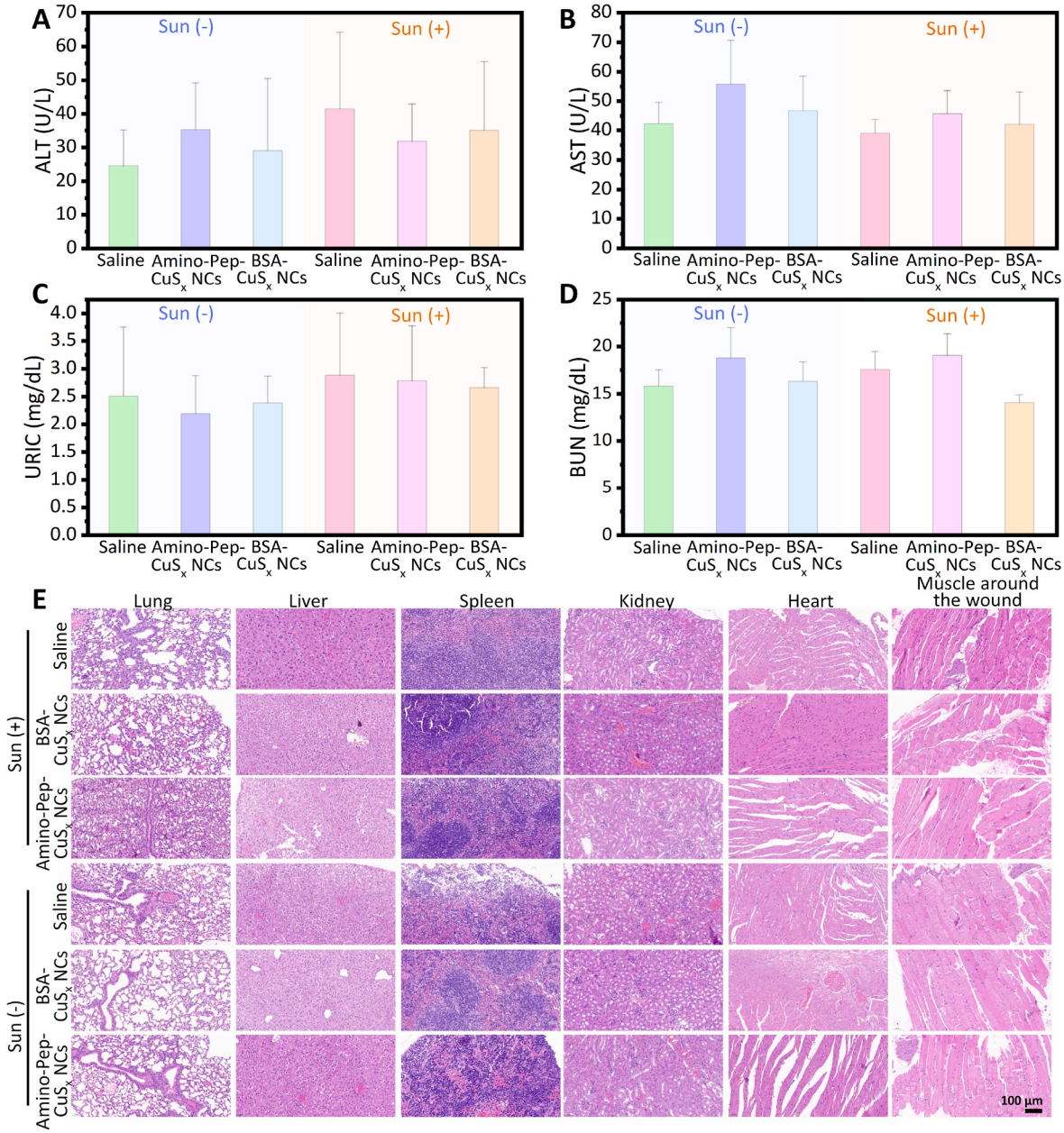

Fig. 8. *In vivo* biosafety of Amino-Pep-CuS_x NCs-2 compared to BSA-CuS_x NCs-2 on C57BL/6J mice. Blood biochemical analysis including alanine aminotransferase (ALT) (**A**), aspartate aminotransferase (AST) (**B**), uric acid (URIC) (**C**), and blood urea nitrogen (BUN) (**D**) of mice treated with Amino-Pep-CuS_x NCs-2 and BSA-CuS_x NCs-2 with and without sunlight irradiation; (**E**) The H&E staining of main organs and peri-wound muscles of mice treated by different groups.

CuS_x NCs, which complied with the *in vivo* cell viability data. In summary, the light-irradiated activated Amino-Pep-CuS_x NCs demonstrated the most effective healing outcome, showcasing a faster wound healing rate attributed to a combination of enhanced phagocytic activity and a synergistic hyperthermia-induced chemodynamic effect.

To further assess the biosafety of Amino-Pep-CuS_x NCs and BSA-CuS_x NCs, the biochemical analysis [52–54] on the blood of different groups of mice were conducted. Liver and kidney indexes, including alanine transaminase (ALT), aspartate transaminase (AST), blood urea nitrogen (BUN), and uric acid (URIC), were tested. The results revealed no notable discrepancy compared to those in the control group, indicating the negligible liver and kidney burden of CuS_x NCs (Fig. 8A–D). Moreover, blood cells, blood biochemistry, and visceral sections of mice from various groups were examined and compared. Examination of hematocrit, hemoglobin (Table S1), platelets (Table S2), and various immune cells (Table S3) in mice treated with CuS_x NCs revealed similar values to the control groups for all parameters. This suggests that sun irradiation had no discernible impact on blood cells in mice treated with CuS_x NCs, both with and without sunlight exposure. To further confirm the favorable biosafety of CuS_x NCs, all groups were euthanized on day 13, and various organs were subjected to histological analysis using hematoxylin and eosin (H&E) staining. As depicted in Fig. 8E, there were no remarkable histopathological abnormalities or lesions detected in all organs including heart, liver, spleen, lung, or kidney of mice treated with CuS_x NCs, regardless of sun irradiation. This suggests that the utilization of Amino-Pep-CuS_x NCs and BSA-CuS_x NCs on the skin surface does not result in any discernible organic damage to major organs. Furthermore, there were no apparent signs of apoptosis or necrosis, and the diminished reproductive capacity of muscle tissue near the wound indicated no adverse effects of CuS_x NCs, even when exposed to sunlight. In summary, these findings unequivocally establish that CuS_x NCs pose no risk of harm to normal tissues during the therapeutic process, affirming their exceptional biosafety.

4. Conclusion

In summary, we have innovatively designed Amino-Pep-wrapped CuS_x nanoclusters (Amino-Pep-CuS_x NCs) to achieve an augmented synergistic photothermal-chemodynamic therapy for infected wounds. This is accomplished through an actively engaging "swallowing" effect, wherein the nanoclusters act as a bacterial food source. Defect engineering of CuS_x NCs, prepared through a straightforward room-temperature approach, was implemented to modulate their performance in PTT and CDT. This was achieved by adjusting the sulfur vacancy density on the surface, allowing for tunable therapeutic capabilities. These CuS_x NCs demonstrated a trend of decreasing photothermal-induced heat and increasing Fenton-like activity-induced HO• generation as the sulfur defect density increased. The partial and gradual biodegradability of CuS_x NCs into copper ions both increased the ROS production by enhancing sulfur defects, and potentially aided in the eventual removal of CuS_x NCs from the body after achieving their therapeutic effects. The XPS results validated that the sulfur defect increased proportionally with the rise in Cu^+ content, leading to enhanced HO• generation, suggesting that the chemodynamic effect can be precisely fine-tuned by managing the intrinsic valence state of copper in CuS_x NCs. Owing to the presence of Amino-Pep derived from bacterial medium, Amino-Pep-CuS_x NCs were actively consumed as "food" by bacteria, resulting in higher bacterial uptake efficiency. This, in turn, led to a more pronounced synergistic therapeutic effect against bacteria, achieved through the combined utilization of photothermal performance and chemodynamic effects. Therefore, the devised strategy demonstrates an exceptionally high *in vivo* broad-spectrum antibacterial performance, surpassing approximately 98.0 % on the infected wound site during the treatment process. Considering its outstanding biocompatibility and biosafety, this effective approach not only reveals alternative design guidelines for enhancing hyperthermia-assisted CDT but also holds great promise for advancing the study of bacteria inhibition in infected wounds. Furthermore, it holds promise for the advancement of novel diagnostic and therapeutic agents.

Ethics approval and consent to participate

Animal ethics approval was obtained from Laboratory Animal Welfare Ethics Committee of Central South University.

CRediT authorship contribution statement

Maonan Wang: Writing – original draft, Visualization, Validation, Software, Resources, Methodology, Investigation, Formal analysis, Data curation. **Houjuan Zhu:** Writing – review & editing, Writing – original draft, Visualization, Validation, Supervision, Software, Resources, Methodology, Investigation, Funding acquisition, Formal analysis, Data curation, Conceptualization. **Yuling Xue:** Investigation, Formal analysis. **Yanxia Duan:** Validation, Data curation. **Hua Tian:** Investigation, Formal analysis. **Qi Liu:** Investigation, Data curation. **Yuzhu Zhang:** Investigation, Data curation. **Zibiao Li:** Supervision, Resources, Investigation. **Xian Jun Loh:** Resources, Investigation. **Enyi Ye:** Resources, Investigation. **Gang Yin:** Resources. **Xuemei Wang:** Resources. **Xianguang Ding:** Investigation. **David Tai Leong:** Writing – review & editing, Visualization, Supervision, Investigation, Funding acquisition, Conceptualization.

Declaration of competing interest

David Tai Leong is an associate editor for Bioactive Materials and was not involved in the editorial review or the decision to publish this article. All authors declare that there are no competing interests.

Acknowledgments

We acknowledge the funding provided by the National University of Singapore Reimagine Grant (A-0009179-02-00; A-0009179-03-00); National Natural Science Foundation of China (82303841), Hunan Provincial Natural Science Foundation (2023JJ40800), and the program of China Scholarships Council (No.202006090323).

Appendix A. Supplementary data

Supplementary data to this article can be found online at https://doi.org/10.1016/j.bioactmat.2024.09.010.

References

[1] A. Assié, B.S. Samuel, The devil is in the microbial genetic details, Mol. Cell 74 (6) (2019) 1108–1109.
[2] L.X. Yip, J. Wang, Y. Xue, K. Xing, C. Sevencan, K. Ariga, D.T. Leong, Cell-derived nanomaterials for biomedical applications, Sci. Technol. Adv. Mater. 25 (1) (2024) 2315013.
[3] K. Ariga, Nanoarchitectonics: the method for everything in materials science, Bull. Chem. Soc. Jpn. 97 (1) (2024) uoad001.
[4] X. Lan, H. Zhang, H. Qi, S. Liu, X. Zhang, L. Zhang, Custom-design of triblock protein as versatile antibacterial and biocompatible coating, Chem. Eng. J. 454 (2023) 140185.
[5] S. Wan, K. Wang, P. Huang, X. Guo, W. Liu, Y. Li, J. Zhang, Z. Li, J. Song, W. Yang, X. Zhang, X. Ding, D.T. Leong, L. Wang, Mechanoelectronic stimulation of autologous extracellular vesicle biosynthesis implant for gut microbiota modulation, Nat. Commun. 15 (1) (2024) 3343.
[6] H. Tian, H. Zhu, Y. Xue, M. Wang, K. Xing, Z. Li, X.J. Loh, E. Ye, X. Ding, B.L. Li, X. Yin, D.T. Leong, White light powered antimicrobial nanoagents for triple photothermal, chemodynamic and photodynamic based sterilization, Nanoscale Horiz. 9 (2024) 1190–1199..
[7] E. Deriu, Janet Z. Liu, M. Pezeshki, Robert A. Edwards, Roxanna J. Ochoa, H. Contreras, Stephen J. Libby, Ferric C. Fang, M. Raffatellu, Probiotic bacteria reduce Salmonella typhimurium intestinal colonization by competing for iron, Cell Host Microbe 14 (1) (2013) 26–37.
[8] J.L. Lister, A.R. Horswill, Staphylococcus aureus biofilms: recent developments in biofilm dispersal, Front. Cell. Infect. Microbiol. 4 (2014) 178.

[9] K.S. Singh, R. Sharma, P.A.N. Reddy, P. Vonteddu, M. Good, A. Sundarrajan, H. Choi, K. Muthumani, A. Kossenkov, A.R. Goldman, H.-Y. Tang, M. Totrov, J. Cassel, M.E. Murphy, R. Somasundaram, M. Herlyn, J.M. Salvino, F. Dotiwala, IspH inhibitors kill Gram-negative bacteria and mobilize immune clearance, Nature (London) 589 (7843) (2021), 597-5.

[10] Y. Jin, H. Liu, L. Chu, J. Yang, X. Li, H. Zhou, H. Jiang, L. Shi, J. Weeks, J. Rainbolt, C. Yang, T. Xue, H. Pan, Z. Deng, C. Xie, X. Cui, Y. Ren, Initial therapeutic evidence of a borosilicate bioactive glass (BSG) and Fe_3O_4 magnetic nanoparticle scaffold on implant-associated Staphylococcal aureus bone infection, Bioact. Mater. 40 (2024) 148–167.

[11] G. Chu, M. Guan, J. Jin, Y. Luo, Z. Luo, T. Shi, T. Liu, C. Zhang, Y. Wang, Mechanochemically reprogrammed interface orchestrates neutrophil bactericidal activity and apoptosis for preventing implant-associated infection, Adv. Mater. (2024) 2311855.

[12] J. Zhao, S. Huang, P. Ravisankar, H. Zhu, Two-dimensional nanomaterials for photoinduced antibacterial applications, ACS Appl. Bio Mater. 3 (12) (2020) 8188–8210.

[13] Y. Feng, Z. Qin, Y. Geng, X. Huang, P. Ouyang, D. Chen, H. Guo, H. Deng, W. Lai, Z. Zuo, J. Fang, Z. Zhong, Regional analysis of the characteristics and potential risks of bacterial pathogen resistance under high-pressure antibiotic application, J. Environ. Manag. 317 (2022) 115481.

[14] C.K.C. Lai, R.W.Y. Ng, S.S.Y. Leung, M. Hui, M. Ip, Overcoming the rising incidence and evolving mechanisms of antibiotic resistance by novel drug delivery approaches – an overview, Adv. Drug Deliv. Rev. 181 (2022) 114078.

[15] H.M. Wong, Y.Y. Zhang, Q.L. Li, An enamel-inspired bioactive material with multiscale structure and antibacterial adhesion property, Bioact. Mater. 7 (2022) 491–503.

[16] M.-C. Wu, A.R. Deokar, J.-H. Liao, P.-Y. Shih, Y.-C. Ling, Graphene-based photothermal agent for rapid and effective killing of bacteria, ACS Nano 7 (2) (2013) 1281–1290.

[17] X. Dai, Z. Fan, Y. Lu, P.C. Ray, Multifunctional nanoplatforms for targeted multidrug-resistant-bacteria theranostic applications, ACS Appl. Mater. Inter. 5 (21) (2013) 11348–11354.

[18] S. Wu, J. Xu, L. Zou, S. Luo, R. Yao, B. Zheng, G. Liang, D. Wu, Y. Li, Long-lasting renewable antibacterial porous polymeric coatings enable titanium biomaterials to prevent and treat peri-implant infection, Nat. Commun. 12 (1) (2021) 3303.

[19] Y. Qiao, Y. Xu, X. Liu, Y. Zheng, B. Li, Y. Han, Z. Li, K.W.K. Yeung, Y. Liang, S. Zhu, Z. Cui, S. Wu, Microwave assisted antibacterial action of Garcinia nanoparticles on Gram-negative bacteria, Nat. Commun. 13 (1) (2022) 2461.

[20] W. Zhao, C. Liang, B. Wang, S. Xing, Enhanced photocatalytic and fenton-like performance of CuO_x-decorated $ZnFe_2O_4$, ACS Appl. Mater. Inter. 9 (48) (2017) 41927–41936.

[21] Y. Dang, Y. Cheng, Y. Zhou, Y. Huang, K. Wang, Nano-PAA-$CuCl_2$ composite as fenton-like reusable catalyst to enhanced degrade organic pollutant MB/MO, Catalysts (2021).

[22] L. Li, Z. Yang, W. Fan, L. He, C. Cui, J. Zou, W. Tang, O. Jacobson, Z. Wang, G. Niu, S. Hu, X. Chen, In situ polymerized hollow mesoporous organosilica biocatalysis nanoreactor for enhancing ROS-mediated anticancer therapy, Adv. Funct. Mater. 30 (4) (2020) 1907716.

[23] L.-S. Lin, T. Huang, J. Song, X.-Y. Ou, Z. Wang, H. Deng, R. Tian, Y. Liu, J.-F. Wang, Y. Liu, G. Yu, Z. Zhou, S. Wang, G. Niu, H.-H. Yang, X. Chen, Synthesis of copper peroxide nanodots for H_2O_2 self-supplying chemodynamic therapy, J. Am. Chem. Soc. 141 (25) (2019) 9937–9945.

[24] L. Lyu, L. Zhang, C. Hu, Enhanced Fenton-like degradation of pharmaceuticals over framework copper species in copper-doped mesoporous silica microspheres, Chem. Eng. J. 274 (2015) 298–306.

[25] D.A. Nichela, A.M. Berkovic, M.R. Costante, M.P. Juliarena, F.S. García Einschlag, Nitrobenzene degradation in Fenton-like systems using Cu(II) as catalyst. Comparison between Cu(II)- and Fe(III)-based systems, Chem. Eng. J. 228 (2013) 1148–1157.

[26] H. Zhu, S. Huang, M. Ding, Z. Li, J. Li, S. Wang, D.T. Leong, Sulfur defect-engineered biodegradable cobalt sulfide quantum dot-driven photothermal and chemodynamic anticancer therapy, ACS Appl. Mater. Inter. 14 (22) (2022) 25183–25196.

[27] X. Liu, Y. Liu, J. Wang, T. Wei, Z. Dai, Mild hyperthermia-enhanced enzyme-mediated tumor cell chemodynamic therapy, ACS Appl. Mater. Inter. 11 (26) (2019) 23065–23071.

[28] H. Zhu, J. Mah Jian Qiang, C.G. Wang, C.Y. Chan, Q. Zhu, E. Ye, Z. Li, X.J. Loh, Flexible polymeric patch based nanotherapeutics against non-cancer therapy, Bioact. Mater. 18 (2022) 471–491.

[29] X. Guo, X. Zhang, M. Yu, Z. Cheng, Y. Feng, B. Chen, Iron decoration in binary graphene oxide and copper iron sulfide nanocomposites boosting catalytic antibacterial activity in acidic microenvironment against antimicrobial resistance, J. Colloid Interf. Sci. 661 (2024) 802–814.

[30] Y. Feng, Z. Cheng, A.-K.K. Larsen, H. Shi, T. Sun, P. Zhang, M. Dong, L. Liu, Amyloid-like nanofibrous network confined and aligned ultrafine bimetallic nanozymes for smart antibacterial therapy, Materials Today Bio. 22 (2023) 100730.

[31] J. Bai, Y. Feng, W. Li, Z. Cheng, J.M. Rosenholm, H. Yang, G. Pan, H. Zhang, D. Geng, Alternative copper-based single-atom nanozyme with superior multienzyme activities and NIR-II responsiveness to fight against deep tissue infections, Research 6 (2023) 31.

[32] Y. Liu, X. Rong, F. Xie, Y. Lu, J. Zhao, L. Chen, Y.-S. Hu, Unlocking the multi-electron transfer reaction in NASICON-type cathode materials, Materials Futures 2 (2) (2023) 023502.

[33] N. Yang, H. Guo, C. Cao, X. Wang, X. Song, W. Wang, D. Yang, L. Xi, X. Mou, X. Dong, Infection microenvironment-activated nanoparticles for NIR-II photoacoustic imaging-guided photothermal/chemodynamic synergistic anti-infective therapy, Biomaterials 275 (2021) 120918.

[34] X. Lin, Y. Fang, Z. Hao, H. Wu, M. Zhao, S. Wang, Y. Liu, Bacteria-triggered multifunctional hydrogel for localized chemodynamic and low-temperature photothermal sterilization, Small 17 (51) (2021) 2103303.

[35] Y. Liu, W. Chen, W. Mu, Q. Zhou, J. Liu, B. Li, T. Liu, T. Yu, N. Hu, X. Chen, Physiological microenvironment dependent self-cross-linking of multifunctional nanohybrid for prolonged antibacterial therapy via synergistic chemodynamic–photothermal–biological processes, Nano Lett. 24 (23) (2024) 6906–6915.

[36] X. Zhao, H. Tang, X. Jiang, Deploying gold nanomaterials in combating multi-drug-resistant bacteria, ACS Nano 16 (7) (2022) 10066–10087.

[37] Z. Zhang, J. Wen, J. Zhang, D. Guo, Q. Zhang, Vacancy-modulated of CuS for highly antibacterial efficiency via photothermal/photodynamic synergetic therapy, Adv Healthc Mater 12 (1) (2023) 2201746.

[38] Y. Zhong, X.T. Zheng, S. Zhao, X. Su, X.J. Loh, Stimuli-activable metal-bearing nanomaterials and precise on-demand antibacterial strategies, ACS Nano 16 (12) (2022) 19840–19872.

[39] K. Wu, D. Zhu, X. Dai, W. Wang, X. Zhong, Z. Fang, C. Peng, X. Wei, H. Qian, X. Chen, X. Wang, Z. Zha, L. Cheng, Bimetallic oxide Cu1.5Mn1.5O4 cage-like frame nanospheres with triple enzyme-like activities for bacterial-infected wound therapy, Nano Today 43 (2022) 101380.

[40] M. Godoy-Gallardo, U. Eckhard, L.M. Delgado, Y.J.D. de Roo Puente, M. Hoyos-Nogués, F.J. Gil, R.A. Perez, Antibacterial approaches in tissue engineering using metal ions and nanoparticles: from mechanisms to applications, Bioact. Mater. 6 (12) (2021) 4470–4490.

[41] H. Ou, Y. Qian, L. Yuan, H. Li, L. Zhang, S. Chen, M. Zhou, G. Yang, D. Wang, Y. Wang, Spatial position regulation of Cu single atom site realizes efficient nanozyme photocatalytic bactericidal activity, Adv. Mater. 35 (46) (2023) 2305077.

[42] B. Ma, S. Wang, F. Liu, S. Zhang, J. Duan, Z. Li, Y. Kong, Y. Sang, H. Liu, W. Bu, L. Li, Self-assembled copper-amino acid nanoparticles for in situ glutathione "AND" H(2)O(2) sequentially triggered chemodynamic therapy, J. Am. Chem. Soc. 141 (2) (2019) 849–857.

[43] Z. Meng, Y. Chao, X. Zhou, C. Liang, J. Liu, R. Zhang, L. Cheng, K. Yang, W. Pan, M. Zhu, Z. Liu, Near-infrared-triggered in situ gelation system for repeatedly enhanced photothermal brachytherapy with a single dose, ACS Nano 12 (9) (2018) 9412–9422.

[44] J. Ruan, H. Liu, B. Chen, F. Wang, W. Wang, Z. Zha, H. Qian, Z. Miao, J. Sun, T. Tian, Y. He, H. Wang, Interfacially engineered $Zn_xMn_{1-x}S$@Polydopamine hollow nanospheres for glutathione depleting photothermally enhanced chemodynamic therapy, ACS Nano 15 (7) (2021) 11428–11440.

[45] R. Hu, Y. Fang, M. Huo, H. Yao, C. Wang, Y. Chen, R. Wu, Ultrasmall Cu2-xS nanodots as photothermal-enhanced Fenton nanocatalysts for synergistic tumor therapy at NIR-II biowindow, Biomaterials 206 (2019) 101–114.

[46] Y. Wang, L. An, J. Lin, Q. Tian, S. Yang, A hollow Cu_9S_8 theranostic nanoplatform based on a combination of increased active sites and photothermal performance in enhanced chemodynamic therapy, Chem. Eng. J. 385 (2020) 123925.

[47] L.R. Rivera, A. Cochis, S. Biser, E. Canciani, S. Ferraris, L. Rimondini, A. R. Boccaccini, Antibacterial, pro-angiogenic and pro-osteointegrative zein-bioactive glass/copper based coatings for implantable stainless steel aimed at bone healing, Bioact. Mater. 6 (5) (2021) 1479–1490.

[48] Y. Yang, B. Chu, J. Cheng, J. Tang, B. Song, H. Wang, Y. He, Bacteria eat nanoprobes for aggregation-enhanced imaging and killing diverse microorganisms, Nat. Commun. 13 (1) (2022) 1255.

[49] J.-L. Jia, X.-Y. Jin, L. Zhu, Z.-X. Zhang, W.-L. Liang, G.-D. Wang, F. Zheng, X.-Z. Wu, H.-H. Xu, Enhanced intracellular uptake in vitro by glucose-functionalized nanopesticides, New J. Chem. 41 (19) (2017) 11398–11404.

[50] X. Cao, A. Alabresm, Y.P. Chen, A.W. Decho, J. Lead, Improved metal remediation using a combined bacterial and nanoscience approach, Sci. Total Environ. 704 (2020) 135378.

[51] O. Jordan, B.H. Gan, S. Alwan, K. Perron, E. Sublet, V. Ducret, H. Ye, G. Borchard, J.-L. Reymond, V. Patrulea, Highly potent cationic chitosan derivatives coupled to antimicrobial peptide dendrimers to combat Pseudomonas aeruginosa, Adv. Healthc. Mater. (2024) 2304118.

[52] G. Wang, W. Wang, Z. Chen, T. Hu, L. Tu, X. Wang, W. Hu, S. Li, Z. Wang, Photothermal microneedle patch loaded with antimicrobial peptide/MnO_2 hybrid nanoparticles for chronic wound healing, Chem. Eng. J. 482 (2024) 148938.

[53] Z. Wang, Y. Fang, X. Zhou, Z. Li, H. Zhu, F. Du, X. Yuan, Q. Yao, J. Xie, Embedding ultrasmall Ag nanoclusters in Luria-Bertani extract via light irradiation for enhanced antibacterial activity, Nano Res. 13 (1) (2020) 203–208.

[54] X. Ding, F. Peng, J. Zhou, W. Gong, G. Slaven, K.P. Loh, C.T. Lim, D.T. Leong, Defect engineered bioactive transition metals dichalcogenides quantum dots, Nat. Commun. 10 (1) (2019) 41.

[55] H. Zhu, W. Zan, W. Chen, W. Jiang, X. Ding, B.L. Li, Y. Mu, L. Wang, S. Garaj, D. T. Leong, Defect-rich molybdenum sulfide quantum dots for amplified photoluminescence and photonics-driven reactive oxygen species generation, Adv. Mater. 34 (31) (2022) e2200004.

[56] R. Doolen, R. Laitinen, F. Parsapour, D.F. Kelley, Trap state dynamics in MoS_2 nanoclusters, J. Phys. Chem. B 102 (20) (1998) 3906–3911.

[57] B. Ma, S. Wang, F. Liu, S. Zhang, J. Duan, Z. Li, Y. Kong, Y. Sang, H. Liu, W. Bu, L. Li, Self-assembled copper–amino acid nanoparticles for in situ glutathione "AND" H_2O_2 sequentially triggered chemodynamic therapy, J. Am. Chem. Soc. 141 (2) (2019) 849–857.

[58] H. Sun, O.A. Zelekew, X. Chen, Y. Guo, D.-H. Kuo, Q. Lu, J. Lin, A noble bimetal oxysulfide CuVOS catalyst for highly efficient catalytic reduction of 4-nitrophenol and organic dyes, RSC Adv. 9 (55) (2019) 31828–31839.
[59] X. Liu, Z. Yan, Y. Zhang, Z. Liu, Y. Sun, J. Ren, X. Qu, Two-dimensional metal–organic framework/enzyme hybrid nanocatalyst as a benign and self-activated cascade reagent for in vivo wound healing, ACS Nano 13 (5) (2019) 5222–5230.
[60] Y. Han, S. Gao, Y. Zhang, Q. Ni, Z. Li, X.J. Liang, J. Zhang, Metal-based nanocatalyst for combined cancer therapeutics, Bioconjug. Chem. 31 (5) (2020) 1247–1258.
[61] L.S. Lin, T. Huang, J. Song, X.Y. Ou, Z. Wang, H. Deng, R. Tian, Y. Liu, J.F. Wang, Y. Liu, G. Yu, Z. Zhou, S. Wang, G. Niu, H.H. Yang, X. Chen, Synthesis of copper peroxide nanodots for H(2)O(2) self-supplying chemodynamic therapy, J. Am. Chem. Soc. 141 (25) (2019) 9937–9945.
[62] L.H. Fu, C. Qi, J. Lin, P. Huang, Catalytic chemistry of glucose oxidase in cancer diagnosis and treatment, Chem. Soc. Rev. 47 (17) (2018) 6454–6472.
[63] P. Chen, Y. Ma, Z. Zheng, C. Wu, Y. Wang, G. Liang, Facile syntheses of conjugated polymers for photothermal tumour therapy, Nat. Commun. 10 (1) (2019) 1192.
[64] X. Jin, G. Lin, A. Zeiny, H. Jin, L. Bai, D. Wen, Solar photothermal conversion characteristics of hybrid nanofluids: an experimental and numerical study, Renew. Energy 141 (2019) 937–949.
[65] H. Huang, R. Shi, X. Zhang, J. Zhao, C. Su, T. Zhang, Photothermal-assisted triphase photocatalysis over a multifunctional bilayer paper, Angew. Chem. Int. Ed. 60 (42) (2021) 22963–22969.
[66] H. Zhu, Z. Li, E. Ye, D.T. Leong, Oxygenic enrichment in hybrid ruthenium sulfide nanoclusters for an optimized photothermal effect, ACS Appl. Mater. Inter. 13 (50) (2021) 60351–60361.
[67] H. Liu, Y. Zuo, S. Lv, X. Liu, J. Zhang, C. Zhao, X. Xu, Y. Xu, X. Wang, Ultralow loading copper-intercalated MoO3 nanobelts with high activity against antibiotic-resistant bacteria, ACS Appl. Mater. Inter. 16 (14) (2024) 17182–17192.
[68] M. Xu, Y. Hu, Y. Xiao, Y. Zhang, K. Sun, T. Wu, N. Lv, W. Wang, W. Ding, F. Li, B. Qiu, J. Li, Near-infrared-controlled nanoplatform exploiting photothermal promotion of peroxidase-like and OXD-like activities for potent antibacterial and anti-biofilm therapies, ACS Appl. Mater. Inter. 12 (45) (2020) 50260–50274.
[69] L.-H. Fu, Y. Wan, C. Qi, J. He, C. Li, C. Yang, H. Xu, J. Lin, P. Huang, Nanocatalytic theranostics with glutathione depletion and enhanced reactive oxygen species generation for efficient cancer therapy, Adv. Mater. 33 (7) (2021) 2006892.